



UNIVERSIDADE DE BRASILIA
INSTITUTO DE GEOCIÊNCIAS
PROGRAMA DE PÓS-GRADUAÇÃO EM GEOLOGIA

CAROLINA PEIXOTO DE SOUZA

**MECANISMOS DE DEFORMAÇÃO E GEOCRONOLOGIA U-PB EM
ZIRCÃO DA MILONIZAÇÃO NA PORÇÃO SUL DA ZONA DE
CISALHAMENTO PATOS, PROVÍNCIA BORBOREMA, NE BRASIL**

BRASÍLIA - DF

2021

UNIVERSIDA DE DEBRASÍLIA
INSTITUTO DE GEOCIÊNCIAS
PROGRAMA DE PÓS-GRADUAÇÃO EM GEOLOGIA

**MECANISMOS DE DEFORMAÇÃO E GEOCRONOLOGIA U-PB EM
ZIRCÃO DA MILONIZAÇÃO NA PORÇÃO SUL DA ZONA DE
CISALHAMENTO PATOS, PROVÍNCIA BORBOREMA, NE BRASIL**

DISSERTAÇÃO DE MESTRADO N: 476

Área de Concentração: mineralogia e petrologia

Autora: Carolina Peixoto de Souza
Orientador: Prof. Dr. Luís Gustavo Ferreira Viegas

BRASÍLIA - DF

2021

UNIVERSIDA DE DEBRASÍLIA
INSTITUTO DE GEOCIÊNCIAS
PROGRAMA DE PÓS-GRADUAÇÃO EM GEOLOGIA

**MECANISMOS DE DEFORMAÇÃO E GEOCRONOLOGIA U-PB EM
ZIRCÃO DA MILONIZAÇÃO NA PORÇÃO SUL DA ZONA DE
CISALHAMENTO PATOS, PROVÍNCIA BORBOREMA, NE BRASIL**

Autora: Carolina Peixoto de Souza

Banca Examinadora:

Prof. Dr. Lauro Cézar Montefalco de Lira Santar – Membro Externo Titular – UFPE

Profa. Dra. Catarina Labouré Benfica Toledo – Membro Interno Titular – IG/UnB

BRASÍLIA - DF

2021

Ficha catalográfica elaborada automaticamente,
com os dados fornecidos pelo(a) autor(a)

PC292m Peixoto de Souza, Carolina
Mecanismos de Deformação e Geocronologia U-Pb da Porção
Sul da Zona de Cisalhamento Patos, Província Borborema, NE
Brasil. / Carolina Peixoto de Souza; orientador Luis
Gustavo Ferreira Viegas. -- Brasília, 2021.
62 p.

Dissertação (Mestrado - Mestrado em Geologia) --
Universidade de Brasília, 2021.

1. Zona de Cisalhamento Patos. 2. Magmatismo Granítico .
3. Microestruturas. 4. Geocronologia. 5. Mecanismos de
Deformação. I. Ferreira Viegas, Luis Gustavo, orient. II.
Título.

AGRADECIMENTOS

Agradeço à minha família, mãe, pai e irmã, por todo o apoio ao longo desses dois anos. O incentivo e a certeza do amparo de vocês me fizeram mais resiliente durante todo o processo. Obrigada pela parceria e pelo amor que compartilhamos!

Agradeço ao prof. Gustavo Viegas pela orientação e disponibilidade durante estes dois anos. Muito obrigada por contribuir no meu crescimento científico e geológico e por me ajudar a concluir este processo.

Aos parceiros/as de orientação, Rhander Altoé, Malú Ribeiro e Paulo Castellan, muito obrigada pelas discussões e trocas geológicas, foram de grande importância na construção deste trabalho. Um muito obrigada ao Paulo que me acompanhou no segundo campo e não mediou esforços para que conseguíssemos fazer um ótimo trabalho, além de toda a recepção e acolhida em Recife. E ao Rhander, pela leitura dos meus textos e toda a ajuda, obrigada!

Agradeço ao João Pedro e à Rafaela França da GeoLab pela confecção das lâminas polidas de excelente qualidade.

Agradeço aos trabalhadores e trabalhadoras da UnB que tornam possível a confecção de trabalhos como este. Aos porteiros, seguranças, pessoal da limpeza, técnicos de laboratório, técnicos de informática... muito obrigada!

Obrigada ao Instituto de Geociências da Universidade de Brasília que possibilitou a realização deste trabalho. À todas as professoras e professores que tive a oportunidade de conhecer. Obrigada pelas aulas, campos, conversas e toda troca vivenciada!

Um super obrigada cheio de carinho e boas lembranças às pessoas maravilhosas que conheci em Brasília e que durante esses dois anos me foram família. Levarei um pouquinho de cada uma/um comigo pra sempre.

Por fim, agradeço à Coordenação de Aperfeiçoamento de Pessoal de Nível Superior Brasil (CAPES) pelo apoio e financiamento de todo este projeto. Código de Financiamento: 88882.383270/2019-01.

RESUMO

A porção sul da Zona de Cisalhamento Patos (ZCP), expressivo lineamento da Província Borborema, apresenta rochas miloníticas metamorfizadas principalmente em fácies xisto verde. Estas rochas exibem, localmente, evidências de deformação no estado sólido, o que indica associação com os eventos transcorrentes da ZCP. Ocorrem nesta região embasamento granítico gnáissico, rochas metavulcânicas e metassedimentares neoproterozoicas, além de intrusões graníticas e granodioríticas, como os plútuns Santa Terezinha e Catingueira, dispostos em formas alongadas conforme a foliação milonítica principal. O quartzo recristalizado nestes plútuns apresenta acomodação da deformação por fluência de deslocações, sob fácies xisto verde superior a anfibolito inferior, enquanto que os porfiroclastos e grãos recristalizados de plagioclásio e K-feldspato deformam principalmente por fragmentação mecânica. Os gnaisses graníticos da região exibem condições deformacionais similares às dos plútuns. A orientação preferencial cristalográfica dos cristais de quartzo revela recristalização rotacional ao longo dos planos basal $\langle a \rangle$, rômbico $\langle a+c \rangle$ e prismático $\langle a \rangle$, enquanto que o feldspato ocorre fraturado e heretorgêneo, com deformação no estado sólido localizada nos porfiroclastos. Estas características marcam a coatividade de mecanismos rúpteis e dúcteis durante deformação ao longo do nível crustal intermediário. Dados U-Pb em zircão no plútun Santa Terezinha apresentam idade de 625 ± 7 Ma, interpretada como a idade de cristalização. Tendo em vista a idade de 591 ± 5 Ma apresentada pela literatura para o batólito Teixeira e a idade de cerca de 565 Ma, interpretada como representante do principal evento metamórfico na ZCP, diferentes perspectivas cronológicas para a região são sugeridas. A forma alongada do plútun Santa Terezinha, concordante com a foliação da zona de cisalhamento, bem como a existência de deformação no estado sólido sugerem que sua colocação teve associação com o evento de transcorrência da ZCP. Isto seria possível se o intervalo entre sua geração/colocação e cristalização magmática fosse de aproximadamente 40 Ma. Sucessivos eventos magmáticos podem ter mantido um alto gradiente de temperatura durante o período de cristalização do plútun, contribuindo para um resfriamento lento do corpo.

Palavras-chave: Zona de Cisalhamento Patos, magmatismo granítico, microestruturas, geocronologia, mecanismos de deformação

ABSTRACT

The southern boundary of the Patos Shear Zone (PSZ), an important lineament of the Borborema Province, presents mylonitic rocks that record metamorphism mainly in greenschist facies. These rocks exhibit, locally, solid-state deformation evidence, suggesting an association with the transcurrent events of the PSZ. In this sector occur gneissic granitic basement, Neoproterozoic metavolcanic, and metasedimentary rocks, besides granitic and granodioritic intrusions, as the Santa Terezinha and Catingueira plutons, commonly showing stretched shapes in agreement with the main mylonitic foliation. Recrystallized quartz of these plutons accommodates the deformation by dislocation creep, under upper greenschist facies to lower amphibolite facies, while the porphyroclasts and recrystallized plagioclase and K-feldspar deform by mechanic fragmentation. The granitic gneissic host rocks show similar deformation conditions to the plutons. The OCP of the quartz crystals reveals rotational recrystallization along with the basal $\langle a \rangle$, rhomb $\langle a+c \rangle$, and prismatic $\langle a \rangle$ planes, while the feldspar occurs fractured and heterogeneous, with deformation in solid state in larger porphyroclasts. These characteristics suggest that the deformation occurred at depths equivalent to the brittle-ductile transition, marked by the coactivity of brittle and ductile mechanisms along with the intermediate crustal level. U-Pb zircon data for the Santa Terezinha pluton sample showed an age of 625 ± 7 Ma, interpreted as the age of crystallization. This data, compared to the age of 591 ± 5 Ma presented by the literature for the batholith Teixeira, which occur also in the south of the PSZ, and the age of about 565 Ma interpreted as the main metamorphic event in the PSZ, suggest different perspectives regarding the time of the deformation and magmatism events that occurred at the southern limit of this structure. The elongated shape of the Terezinha pluton in agreement with the shear zone foliation, as well as the existence of deformation in the solid-state suggest that its emplacement had an association with the PSZ transcurrent event. This association would be possible if the interval between the generation/emplacement and magmatic crystallization of the pluton was approximately 40 Ma. Successive magmatic events may have maintained a high-temperature gradient during the pluton crystallization period, contributing to the slow cooling of the body.

Key-words: Patos Shear Zone, granitic magmatism, microstructures, geochronology, deformation mechanisms.

SUMÁRIO

1. INTRODUÇÃO	1
2. GEOLOGIA REGIONAL.....	2
3. MATERIAIS E MÉTODOS.....	5
3.1. Trabalho de campo.....	5
3.2. Descrição petrográfica e microestrutural	6
3.3. Técnicas Analíticas.....	6
3.4. Determinação da Orientação Preferencial Cristalográfica.....	6
3.5. Geocronologia U-Pb em zircão.....	8
3.6. Microssonda Eletrônica.....	10
4. ARTIGO.....	12
4.1. Introduction	13
4.2. Geologic Setting	14
4.3. Methods	17
4.3.1. Field structural mapping	17
4.3.2. Microstructures and EBSD analysis	17
4.3.3. Mineral chemistry	18
4.3.3.1. Zircon U-Pb geochronology	18
4.4. Results	19
4.4.1. Field and petrographic observations.....	19
4.4.2. Microstructure	22
4.4.2.1. Granitic Gneiss.....	22
4.4.2.2. Santa Terezinha Pluton	25
4.4.2.3. Catingueira pluton.....	28
4.4.3. EBSD analysis of quartz CPO in the host mylonites.....	29
4.4.4. Mineral Chemistry.....	31
4.4.5. Zircon U-Pb geochronology.....	36
4.5. Discussion	38
4.5.1. Deformation mechanisms in the mylonitic gneisses.....	38
4.5.2. Mylonitization in the Santa Terezinha and Catingueira plutons	39
4.5.3. Chronology of granitoid magmatism in the southern border of the Patos shear zone	40
4.6. Conclusions	41
5. CONSIDERAÇÕES FINAIS	48
5.1. Caracterização estrutural	48
5.2. Análise temporal do magmatismo granítico na borda sul da Zona de Cisalhamento Patos e suas implicações.....	49

6.	REFERÊNCIAS	50
7.	ANEXOS	54

LISTA DE FIGURAS

Figura 1. Subdivisão da Província Borborema apresentando as idades dos segmentos crustais. Polígono em vermelho representa a área de estudo do presente trabalho. Modificado de Brito Neves <i>et al.</i> 2000; Van Schmus <i>et al.</i> 2008; Santos, 2017. 3	
Figura 2. Mapa gológico esquemático de uma porção da borda sul da Zona de Cisalhamento Patos. Os plútuns Santa Terezinha (ST) e Catingueira (CAT) estão realçados na figura. Modificado de CPRM, Folha SB 24/25 Jaguaribe-Natal, 1981; Archanjo <i>et al.</i> 2008; Viegas <i>et al.</i> 2014.....	5
Figura 3. Esquema do sistema MEV-EBSD e geração de EBSP, apresentando a trajetória entre o feixe de elétrons e a tela fosforescente. Modificado de Morales <i>et al.</i> 2017.....	7
Figura 4. Exemplo de diagrama Concórdia e reta discórdia, modificado de Bühn <i>et al.</i> (2009).	9
Figura 5. Ilustração esquemática de uma microssonda eletrônica, modificado de Goldstein <i>et al.</i> (2003).	11

LISTA DE FIGURES

Figure 1. a) Reconstruction of South-America-Africa exhibiting the Amazonian, São Francisco, West African, and Central Congo Cratons, Brasiliano-Pan-African belts, and Andean Belt. The black square represents the Borborema Province; (b) Schematic map displaying the tectonic domains of Borborema Province (northern, central, and southern) and the main shear zones: SSZ (Sobral Shear Zone); SPSZ (Senador Pompeu Shear Zone); PSZ (Patos Shear Zone); WPSZ (West Pernambuco Shear Zone), and EPSZ (East Pernambuco Shear Zone). The gray square represents the study area; (c) Schematic geological map of the southern Patos Shear Zone, displaying the Paleoproterozoic orthogneisses, migmatites, and amphibolites of the basement, the supracrustal rocks, and Neoproterozoic granites and granodiorites (CAT-Catingueira pluton, ST-Santa Terezinha pluton). The main trend of the mylonitic foliation, mineral stretching lineations, locations of field mapping points (yellow dots), geochronological (blue dot), and EBSD analysis (red stars) samples are shown; (d) Mesoscale structural fabrics (foliation; n=25) and the mineral stretching lineation (n=15) the central-south PSZ. Modified from CPRM, Folha SB 24/25 Jaguaribe-Natal, 1981; Neves *et al.* 2003; Hollanda *et al.* 2010; Archanjo *et al.* 2008; Viegas *et al.* 2014; Castellan *et al.* 2020..... 17

Figure 2. Field aspects of the mylonites and ultramylonites from the southern boundary of the Patos shear zone. (a) Gneissic granite showing fine to coarse-grained mafic and felsic bands, both parallel to the E-W mylonitic foliation of the Patos shear zone. (b) Contact between the mafic and felsic bands of the gneissic granite. The mafic band shows millimetric biotite crystals aligned to the mylonitic foliation, in addition to rounded quartz grains and elongated feldspars. The felsic band presents centimeter-scale porphyroclasts of K-feldspar that are elongated and fractured. A quartz vein parallel to the mylonitic foliation is observed close to the K-feldspar porphyroblast. (c) Fine-grained mafic and felsic bands of the gneissic granite. The felsic bands display K-feldspar porphyroclasts elongated and with augen shapes. (d) Muscovite-rich metapelites. The mylonitic foliation is marked by elongated muscovite and biotite that are aligned with subordinate, stretched K-feldspar porphyroclasts.21

Figure 3. Field aspects of the Santa Terezinha and Catingueira plutons: (a) Santa Terezinha pluton showing a porphyroclastic texture marked by elongated K-feldspar porphyroclasts. The stretched K-feldspar clasts, elongated quartz ribbons and biotite crystals mark the mylonitic foliation. (b) Santa Terezinha pluton presenting centimeter K-feldspar porphyroclasts elongated and developing *augen* morphologies. The porphyroclasts are wrapped by millimeter-scale biotite crystals aligned with the mylonitic foliation. (c) Catingueira pluton showing a light grey color, fine-grained equigranular texture, and a protomylonitic foliation that is evidenced by the preferred orientation of millimetric biotite crystals. (d) Ultramylonite band in Catingueira pluton exhibiting fine-grained biotite and a centimetric quartz vein parallel to the mylonitic foliation.....22

Figure 4. Microstructures of the mylonitic gneisses of the southern Patos shear zone (Qz = quartz, Kfs = K-feldspar, Pl = plagioclase, Bt = biotite, Mtx = matrix; Whitney and Evans, 2010) (a), (b) Overview of typical mylonitic granite with porphyroclasts of K-feldspar and plagioclase wrapped by quartz ribbons and fine-grained recrystallized K-feldspar, plagioclase, quartz and biotite. The mylonitic foliation is defined by the preferred orientation of quartz ribbons, elongated feldspar clasts, and oriented biotite; c), d) Sub-elliptical K-feldspar and plagioclase porphyroblast embedded in the fine-grained recrystallized matrix and showing undulose extinction. A sinistral shear sense defined by asymmetric displacement along oblique microfractures is locally observed in plagioclase clasts [d]; e) Recrystallized grains rimming a K-feldspar clast. The grains are strain-free and have lobate boundaries; f) Rounded and fractured K-feldspar porphyroblast with weak undulose extinction. The fracture crosscuts the clast and originates angular fragments.24

Figure 5. Microstructures of the Santa Teresinha pluton (Pl = plagioclase, Kfs = K-feldspar, Qz = quartz; Whitney and Evans, 2010). (a) Porphyroclasts of feldspar embedded in a fine-grained polyphasic matrix (quartz + feldspar + biotite). Quartz ribbons locally wrap around the clasts; (b) Foliation-parallel quartz ribbons with undulose extinction and straight boundaries that define triple junctions (red arrows); (c) Bookshelf fracturing pattern with dextral shear sense of microfracture set (red arrows) in plagioclase porphyroblast; (d) <i>Augen</i> -shaped K-feldspar porphyroblast displaying intragranular microfracture filled by quartz grains; e), f) Sub-elliptical K-feldspar porphyroclasts displaying microfractures filled by the fine-grained matrix (quartz + feldspars), and surrounded by quartz ribbons and the recrystallized matrix (quartz + feldspars + biotite).....	27
Figure 6. Microstructures of the Catingueira pluton (Qz = quartz, Pl = plagioclase, Kfs = K-feldspar, Amp = amphibole, Bt = biotite, Mtx = fine-grained matrix; Whitney and Evans, 2010). (a) Plagioclase porphyroblast showing a microfracture filled with quartz grains (red arrows) and weak deformation twins. (b) K-feldspar clast with undulose extinction wrapped by coarse-grained polycrystalline quartz aggregates and amphibole crystals changing to biotite (red arrows) parallel to the mylonitic foliation. (c) Quartz ribbons wrapping around plagioclase porphyroclasts. Subgrain boundaries in quartz ribbons are indicated by red arrows. (d) Quartz ribbon displaying straight boundaries and polygonal shapes that define triple junctions. Subgrain boundaries are indicated by red arrows. Amphibole occurs as grains parallel to the ribbon elongation.....	29
Figure 7. EBSD results for the mylonitic fabrics of the southern boundary of Patos shear zone, illustrating pole figures, misorientation axes for low- (2-10°) and high angle (10-45°) boundaries, and misorientation angle distributions. See text for discussion.....	31
Figure 8. Chemical composition of K-feldspar and plagioclase porphyroclasts and recrystallized matrix: (a,b) Santa Terezinha pluton (c,d) Catingueira pluton.	32
Figure 9. Feldspar classification diagrams for the (a) Santa Terezinha pluton and (b) Catingueira pluton.	33
Figure 10. (a) Backscatter electron images of zircon grains from samples PUR-02D, Santa Terezinha pluton. (b) Concordia plot for the PUR-02C zircon spots with a lower 5% discordance displaying the main age of 625 ± 7 Ma.	36

LISTA DE TABELAS

Tabela 1. Representative major element chemical analyses for the Santa Terezinha pluton..33

Tabela 2. Representative chemical analyses for the Catingueira pluton.....	35
Tabela 3. LA-MC-ICP-MS U-Pb data used for U-Pb age calculation for the Teresinha pluton.....	37

ESTRUTURA DA DISSERTAÇÃO

Esta dissertação é estruturada em formato de artigo, com o manuscrito a ser submetido organizado no capítulo quatro. O primeiro capítulo, Introdução, consiste na contextualização do tema abordado na pesquisa, discutindo a correlação entre magmatismo e zonas de cisalhamento litosféricas, com destaque para a Província Borborema. No fechamento deste primeiro tópico é indicada a relevância do assunto com base na área de estudo. No segundo capítulo são expostos aspectos da geologia regional com foco para a área de estudo do trabalho. O terceiro capítulo exibe a fundamentação teórica das técnicas analíticas aqui utilizadas. No quarto capítulo apresentamos um compilado dos principais resultados adquiridos neste estudo, os quais foram agrupados em um artigo científico. No quinto capítulo são descritas as considerações finais e discussões geradas a partir dos resultados obtidos neste trabalho. O sexto e último capítulo contém as referências utilizadas.

1. INTRODUÇÃO

A associação entre magmatismo granítico e zonas de cisalhamento registra importantes processos com relação aos eventos deformacionais ocorridos no sistema orogênico ao qual está inserido. As intrusões graníticas comumente apresentam estruturas que marcam os estágios finais da sua exumação e, somadas às características das zonas de cisalhamento próximas, permitem compreender melhor os mecanismos de ascensão destes magmas, bem como a ordem cronológica dos eventos tectônicos ocorridos (Brown & Solar, 1999; Weinberg *et al.* 2004).

Conforme esta associação, os plútuns podem ser interpretados como pré, sin- ou pós-tectônicos no que se refere ao principal evento deformacional ocorrido. Os sin-tectônicos, principalmente, ocorrem em formatos alongados e tabulares, apresentando posicionamento paralelo a levemente oblíquo em relação à orientação das zonas de cisalhamento principais. O tempo de cristalização destes corpos e a natureza da deformação atuante podem ser elucidados sobretudo por meio da morfologia dos plútuns e de suas características estruturais internas, além das texturas relacionadas a eles e às rochas encaixantes (Hutton, 1988; Vigneresse, 1995; Vauchez *et al.* 1997).

A Província Borborema, Nordeste Brasileiro, teve sua evolução tectono-termal marcada por amplo e diverso magmatismo granítico associado a zonas de cisalhamento transcorrentes NE-SW e E-W (Vauchez *et al.* 1995). Três principais eventos magmáticos são reconhecidos: 650 - 625 Ma, 580 - 570 Ma, and 545 - 520 Ma, sendo comum entre estes episódios a correlação cronológica e espacial com importantes zonas de transcorrência próximas (Brito Neves *et al.* 2000; Guimarães *et al.* 2004; Archanjo *et al.* 2008; Hollanda *et al.* 2010).

A Zona de Cisalhamento Patos (ZCP), expressivo lineamento localizado na porção central da Província Borborema, apresenta em sua porção sul rochas gnáissicas, metavulcânicas e metassedimentares intrudidas por plútuns graníticos, as quais ocorrem metamorfizadas principalmente em fácies xisto verde (Corsini *et al.* 1991; Viegas *et al.* 2014). Dentre estes granitóides, os plútuns Santa Terezinha e Catingueira ocorrem em formatos elípticos e alongados conforme a foliação milonítica E-W/NWN. Estes corpos apresentam, localmente, evidências de deformação no estado sólido, indicando uma possível associação com os eventos transcorrentes da Zona de Cisalhamento Patos (Vauchez *et al.* 1997).

Estudos anteriores interpretam os granitos Santa Terezinha e Catingueira como sendo tardios a posteriores em relação ao Lineamento Patos (Vauchez *et al.* 1997; Britos Neves *et al.* 2003). Apesar disto, dados geocronológicos e de detalhamento estrutural sobre a colocação destes corpos graníticos, bem como a relação da deformação no estado sólido com a deformação de baixo a médio grau ocorrente na porção sul da Zona de Cisalhamento Patos são ainda pouco conhecidos.

Esta dissertação consiste em um estudo estrutural dos milonitos associados ao setor sul da zona de cisalhamento Patos, os quais se desenvolvem essencialmente nos gnaisses graníticos e nos plútuns Santa Terezinha e Catingueira, bem como nas rochas supracrustais adjacentes. Por meio de mapeamento estrutural de campo, detalhamento microestrutural e determinações geocronológicas são discutidos os mecanismos de deformação que atuaram durante a colocação dos plútuns, como também a cronologia entre os eventos de magmatismo e deformação no setor sul da estrutura. O presente banco de dados produzido nesta dissertação permite discutir em maior detalhe os processos de cristalização dos plútuns e suas relações com o principal evento de metamorfismo estabelecido para a zona de cisalhamento Patos.

2. GEOLOGIA REGIONAL

A Província Borborema foi definida por Almeida *et al.* (1981) como a região Pré-Cambriana localizada na porção NE da Plataforma Sul-Americana. É limitada ao norte e ao sul pelos cráttons São Luis e São Francisco respectivamente, à leste pelas bacias costeiras (Sergipe-Alagoas, Paraíba e Potiguar) e à oeste pela Bacia Parnaíba (Figura 1). Ao longo da Província ocorrem núcleos arqueanos, ortognaisses e migmatitos paleoproterozoicos, cinturões de rochas supracrustais estaterianas e meso- a neoproterozoicas, além de um amplo e diverso magmatismo expresso na forma de plútuns graníticos (Almeida *et al.* 1967; Van Schmus *et al.*, 2008; Brito Neves *et al.*, 2014).

Durante a orogenia Brasiliana, ocorrida no Neoproterozoico por volta de 600 Ma, consecutivos eventos de deformação e metamorfismo culminaram em um sistema de zonas de cisalhamento em escala continental, ao longo de 200.000 km², associado ao magmatismo granítico (Vauchez *et al.* 1995; Corsini *et al.* 1998; Brito Neves *et al.* 2003). Estas zonas de cisalhamento, sobretudo E-W, dividem os principais domínios geotectônicos que compõem a Província Borborema, os quais são de norte para sul: Médio Coreaú, Ceará Central, Rio Grande do Norte, Transversal e Meridional (Brito Neves *et al.* 2000; Figura 1).

Dentre os sistemas de cisalhamento existentes na Província Borborema, o Sistema Patos-Seridó, situado na porção centro-leste da província, é constituído pela Zona de Cisalhamento Patos e pelas rochas metassedimentares da Faixa Seridó (Corsini *et al.* 1991; 1996). O lineamento Patos se estende por cerca de 600 km na direção E-W e divide os domínios geotectônicos Norte e Transversal da Província Borborema (Van Schmus *et al.* 2011). O domínio Norte compreende rochas paleoproterozoicas do embasamento, núcleos arqueanos e supracrustais neoproterozoicos, além de plútões graníticos ediacaranos (Van Schmus *et al.* 2011). O domínio Transversal ocorre entre as zonas de cisalhamento Patos e Pernambuco e é composto sobretudo pela Zona Transversal, a qual é dividida de leste para oeste entre os terrenos Rio Capibaribe, Alto Moxotó, Alto Pajeú e Piancó Alto-Brígida ou faixa Cachoeirinha (Santos e Medeiros 1999; Brito Neves *et al.*, 2000; Kozuch 2003; Van Schmus *et al.* 2011).

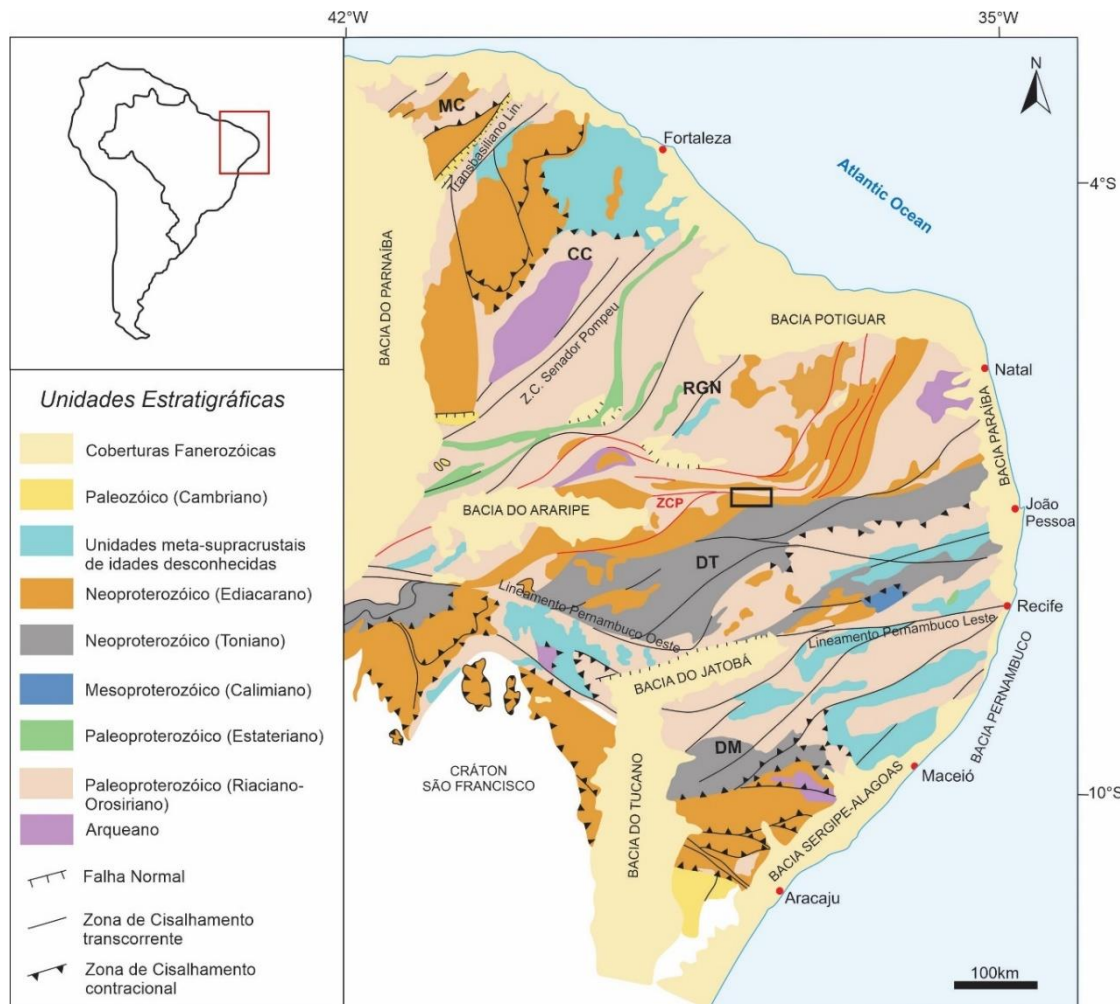


Figura 1. Subdivisão da Província Borborema apresentando as idades dos segmentos crustais. Domínios: MC- Médio Coreau Domínio; CC: Ceará Central; RGN: Rio Grande do Norte; DT: Transversal; DM: Meridional. Polígono em preto representa a área de estudo do presente trabalho, localizada a sul da Zona de Cisalhamento Patos (ZCP), realçada em vermelho. Modificado de Brito Neves *et al.* 2000; Van Schmus *et al.* 2008; Santos, 2017.

A ZCP é caracterizada como uma estrutura transcorrente dextral e apresenta nos setores norte e central migmatitos e milonitos de alta temperatura com evidências de fusão parcial e metamorfismo em fácies anfibolito. Estritamente na porção sul do lineamento ocorrem rochas miloníticas que registram metamorfismo principalmente em fácies xisto verde (Corsini *et al.* 1991; Viegas *et al.* 2014). Recentemente, por meio do método U-Pb SHRIMP em zircão, Viegas *et al.* (2014) apresentaram e interpretaram a idade de 566 ± 6 Ma obtida em leucogranitos associados aos diatextos na porção central do lineamento como a idade do pico metamórfico (associado à migmatização) ocorrido na ZCP.

Na porção sul do lineamento ocorrem embasamento granítico gnáissico, rochas supracrustais neoproterozoicas, além de intrusões graníticas e granodioríticas comumente alongadas conforme a foliação principal E-W ((Figura 2; Corsini *et al.* 1991; Archanjo *et al.* 2008). Dentre estes granitóides, os plútuns Catingueira e Santa Terezinha exibem cerca de 1 km de largura e 10 km de comprimento e intrudem as rochas metassedimentares e metavulcânicas da faixa Cachoeirinha (Terreno Piancó Alto-Brígida; Vauchez *et al.* 1997).

A intrusão dos plútuns Santa Terezinha e Catingueira é considerada por alguns autores como tardia ou pós-cinemática com relação ao principal evento de transcorrência da Zona de Cisalhamento Patos (Almeida *et al* 1967; Sial, 1986; Brito Neves *et al* 2003, Vauchez *et al*, 1997). Brito Neves *et al.* (2003), por meio do método U-Pb em zircão em sienogranitos, apresentaram uma idade de 573 ± 45 Ma para o plúton Catingueira, além de dados Sm/Nd de $T_{DM}=2397$ Ma e $\epsilon_{Nd600}=-15,65$, sugerindo fontes Paleoproterozoicas para este granito.

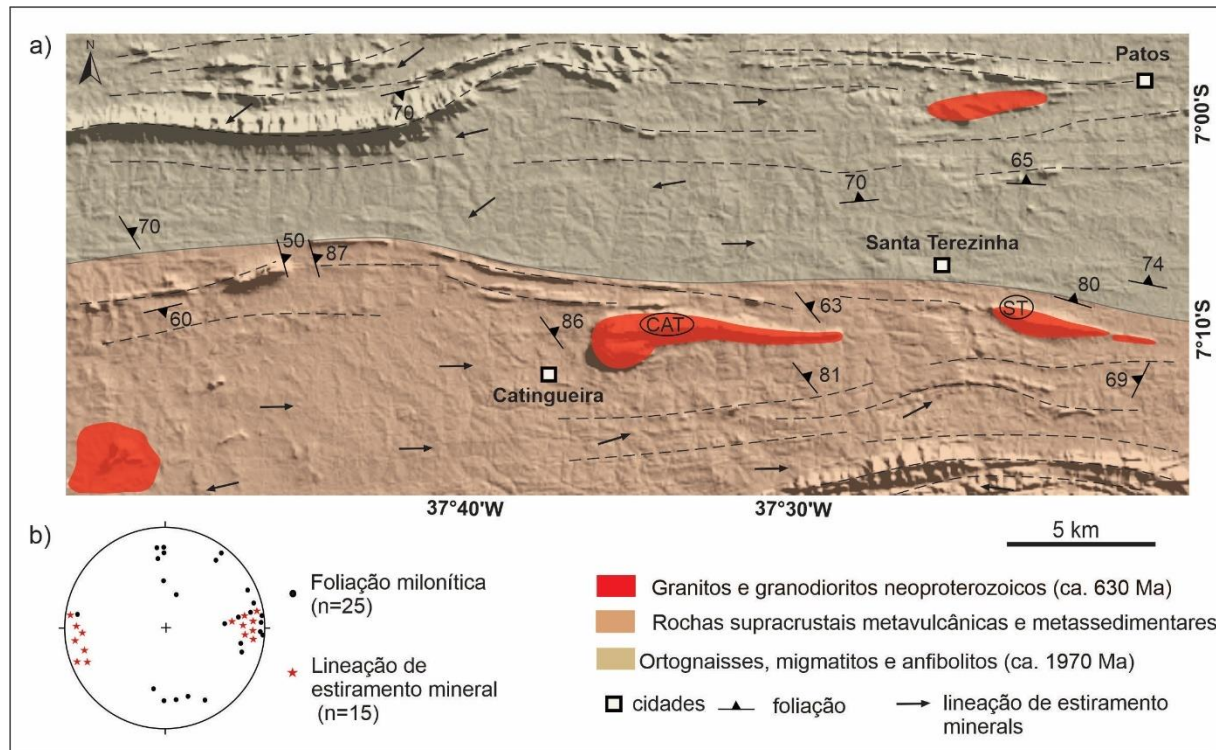


Figura 2. Mapa geológico esquemático da borda sul da Zona de Cisalhamento Patos. Os plútôns Santa Terezinha (ST) e Catingueira (CAT) estão realçados na figura. Modificado de CPRM, Folha SB 24/25 Jaguaribe-Natal, 1981; Archanjo *et al.* 2008; Viegas *et al.* 2014.

3. MATERIAIS E MÉTODOS

3.1. Trabalho de campo

O trabalho de campo foi realizado ao longo da borda sul da Zona de Cisalhamento Patos (Figura 2), entre a cidade de Patos e proximidades da cidade de Coremas, com o objetivo de cartografar e identificar as ocorrências de corpos graníticos com evidências de deformação de baixa temperatura, bem como registros desta deformação nas rochas encaixantes. Nestes corpos foram observadas as principais estruturas, relações geométricas e critérios cinemáticos existentes. Em todos os afloramentos, amostras representativas da deformação local foram coletadas e orientadas em relação à sua foliação e lineação.

Durante o trabalho de campo, feições estruturais dos afloramentos foram observadas, como a intensidade da deformação dos corpos e sua relação com as rochas do entorno, textura e identificação dos minerais (clastos e matriz), além de evidências do grau metamórfico relacionado à intensidade de deformação presente nos corpos rochosos.

3.2.Descrição petrográfica e microestrutural

Foram selecionadas 23 amostras para análise e detalhamento petrográfico, as quais foram cortadas paralelas ao plano XZ para confecção das lâminas polidas. A descrição petrográfica e o registro fotográfico ocorreram no Laboratório de Microscopia do Instituto de Geociências – UnB.

O foco da investigação microestrutural foi a caracterização da geometria entre as fases minerais, distribuição e tamanho dos grãos, além de morfologia e indícios de deformação rúptil existentes. Investigou-se também, por meio das texturas ocorrentes e do contato entre os grãos, possíveis evidências de processos de recristalização. Esta análise mais detalhada, possibilitou uma melhor identificação dos padrões microestruturais existente nos plútons Catingueira e Santa Terezinha, identificação esta muitas vezes prejudicada em campo devido à foliação ocorrer de forma incipiente na maioria dos afloramentos visitados.

3.3.Técnicas Analíticas

Esta pesquisa foi desenvolvida por meio da integração de métodos qualitativos e quantitativos relacionados principalmente à geologia estrutural. De início, realizou-se trabalho de campo com foco na descrição das estruturas deformacionais nos afloramentos ocorrentes na porção sul da Zona de Cisalhamento Patos. As técnicas analíticas utilizadas foram: (a) microscopia ótica; (b) uso da técnica de difração de elétrons retro-espalhados (*Electron Backscattered Diffraction*, EBSD), para determinação da orientação preferencial cristalográfica (OPC) das fases deformadas; (c) Geocronologia U-Pb em zircão e (d) análise da química mineral com microssonda eletrônica por meio da Espectroscopia dispersiva de comprimento de onda (*Wavelength Dispersive Spectroscopy*, WDS).

3.4.Determinação da Orientação Preferencial Cristalográfica

Por meio da técnica de difração de elétrons retroespalhados, o feixe de elétrons produzido pelo MEV pode ser utilizado para a aquisição das Orientações Preferenciais Cristalográficas (OPCs). Ao MEV é acoplada uma tela fosforescente, na qual ocorrerá a projeção dos padrões de elétrons retroespalhados (*Electron Backscatter Patterns*, EBSPs), uma câmera de baixa luminosidade e um computador com software de controle e processamento de dados (Figura 3; Morales *et al.* 2007).

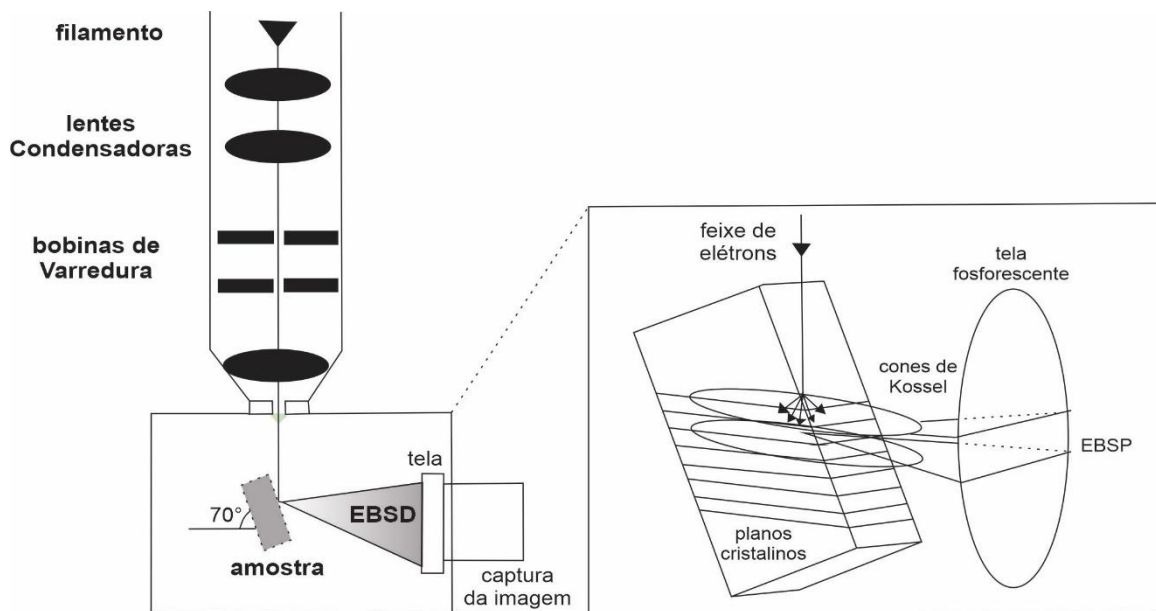


Figura 3. Esquema do sistema MEV-EBSD e geração de EBSPs, apresentando a trajetória entre o feixe de elétrons e a tela fosforescente. Modificado de Morales *et al.* 2017

A mostra é colocada na câmara de vácuo com uma inclinação de cerca de 70° com relação à horizontal. Ao incidir o feixe de elétrons na amostra (ca. 20 kV), os elétrons são dispersados e retroespalhados conforme a direção dos planos cristalográficos da amostra em análise, obedecendo a Lei de Bragg (1). Estes elétrons descrevem então uma trajetória cônica, definida pelos cones de *Kossel*, os quais são interceptados em uma tela fosforescente formando faixas ou linhas denominadas bandas de *Kikuchi* (Figura 3; Prior *et al.*, 1999; Morales *et al.* 2007). A lei de Bragg pode ser definida como:

$$2d_{hkl} \sin\theta = n \lambda \quad (1)$$

Onde:

d_{hkl} = distância reticular (hkl),

θ = ângulo de Bragg,

n = ordem de reflexão,

λ = comprimento de onda relacionado a tensão de aceleração dos elétrons.

As bandas de *Kikuchi* possuem padrão paralelo e são caracterizadas por linhas que possuem um espaçamento distal de 2θ . Este ângulo distal é correlacionado aos ângulos entre os planos reticulares e a interseção entre as bandas caracteriza uma direção cristalográfica. Dessa

forma, a orientação da interseção entre diversos conjuntos de bandas de *Kikuchi* pode ser usada para determinar a orientação preferencial cristalográfica dos minerais (Morales *et al.*, 2007).

As OPCs, identificadas por meio do método de EBSD, são geralmente apresentadas em figuras de polo, as quais representam os eixos tridimensionais dos minerais em duas dimensões (Randle e Caul, 1996). Estas figuras são expressas como estereogramas orientados de acordo com a foliação e a lineação da rocha em análise, apresentando os polos dos planos da rede cristalográfica de um determinado mineral. Por meio das OPCs obtidas, informações quanto às condições de deformação do mineral podem ser interpretadas, tais como: deformação coaxial ou não-coaxial, mecanismos de deformação e estimativa da temperatura de deformação. Em conjunto com demais informações microestruturais, os dados obtidos por meio da análise das OPCs são de grande importância para uma melhor compreensão das condições de deformação de determinada rocha (Wenk e Christie, 1991).

Neste trabalho, as análises EBSD foram realizadas com a amostra posicionada em um ângulo de $\sim 70^\circ$ em relação ao feixe do MEV, o qual operou com tensão de aceleração igual a 20 keV, intensidade de corrente de 15 μA e uma distância de trabalho de ~ 20 mm.

3.5. Geocronologia U-Pb em zircão

Por meio das séries de decaimento dos isótopos radioativos instáveis (pai) U^{238} , U^{235} e Th^{232} para os isótopos radiogênicos estáveis (filho) Pb^{206} , Pb^{207} e Pb^{208} são obtidas informações sobre a idade de cristalização de determinado mineral, bem como de um processo ao qual de investiga (Buhn *et al.* 2009; Dickin, 1997).

Para o caso de dois isótopos radioativos de um mesmo elemento, como é o caso do sistema de decaimento do U^{238} e do U^{235} , as proporções entre os produtos estáveis do decaimento e dos isótopos pais ($\text{Pb}^{206}/\text{U}^{238}$ e $\text{Pb}^{207}/\text{U}^{235}$) são correlacionados por meio da equação abaixo, sendo λ a constante de decaimento do respectivo isótopo radioativo (Buhn *et al.* 2009):

$$\frac{\text{Pb}^{206}}{\text{U}^{238}} = (\frac{\text{Pb}^{207}}{\text{U}^{235}} + 1)\lambda \text{U}^{238} / \lambda \text{U}^{235} \quad (2)$$

Por meio desta relação é obtido então o diagrama ou a curva concórdia (Figura 4), a qual é caracterizada por ser uma representação geométrica do diagrama $\text{Pb}^{206}/\text{U}^{238}$ versus $\text{Pb}^{207}/\text{U}^{235}$ onde ficam os pontos obtidos de idades com valores correspondentes. Quando ocorre

perda de Pb no sistema devido a fatores como intemperismo químico, hidrotermalismo e metamorfismo, os pontos analíticos não coincidem com a concórdia quando lançados no diagrama e formam, então, a reta discórdia (Dickin, 1997). Em casos de perda de Pb por eventos metamórficos posteriores à cristalização do mineral ou rocha, a reta da discórdia intercepta a curva concórdia nas porções inferior e superior. Pode-se interpretar, então, o intercepto superior como a idade de cristalização e o intercepto inferior como a idade do evento metamórfico (Dickin, 1997; Bühn *et al.* 2009).

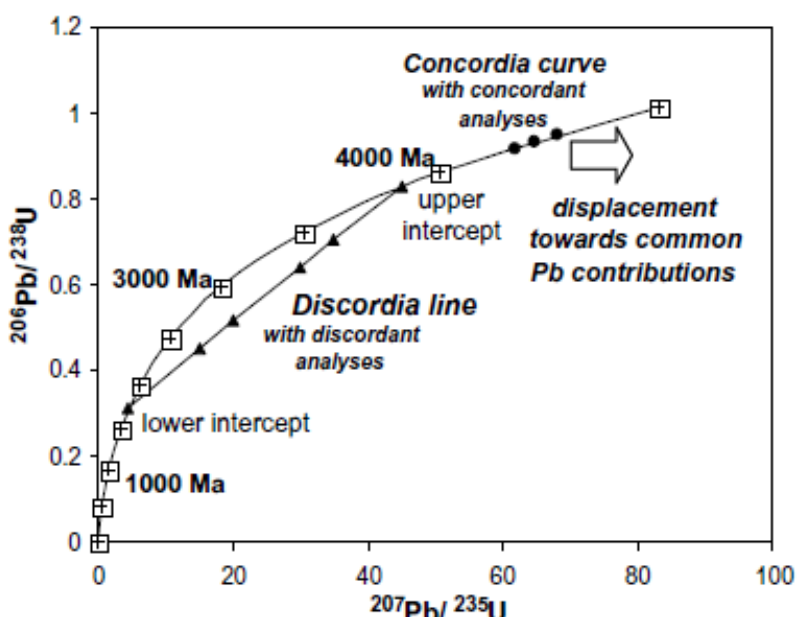


Figura 4. Exemplo de diagrama Concórdia e reta discórdia, modificado de Bühn *et al.* (2009).

O zircão (ZrSiO_4) é um mineral amplamente utilizado no método U-Pb devido à sua grande distribuição e quantidade em diferentes tipos de rochas. Além disso, o zircão aceita facilmente a entrada de U no seu retículo cristalino em substituição ao elemento Zr e ainda, não aceita a entrada de Pb comum, o que faz com que quase a totalidade do Pb existente no mineral seja radiogênico. Outro fator determinante para sua ampla aplicabilidade no método é o fato de o zircão ser extremamente resistente ao intemperismo, o que o torna um mineral ideal devido a pouca perda de Pb e, portanto, resultando numa quantidade menor de idades discordantes (Dickin, 1997).

Neste estudo, os dados geocronológicos foram obtidos utilizando a metodologia de U-Pb descrita por Bühn *et al.* (2009), desenvolvida por meio do espectrômetro de massa *Thermo Finnigan Neptune Multicollector ICP-MS* no Laboratório de Geocronologia da Universidade de Brasília. Foram extraídos em torno de 50 cristais de zircão para amostra representativa do

plúton Santa Terezinha seguindo o procedimento de preparação de amostra padrão, o qual consiste em etapas de britagem, pulverização, concentração por bateia e separação magnética, utilizando separador isodinâmico Frantz.

Os grãos de zircão coletados foram montados em tubos plásticos de 9mm de diâmetro, os quais foram preenchidos com resina e nivelados por meio de polimento para obtenção das análises ICP-MS. Imagens de catodoluminescência (CL) foram obtidas por meio de microscópio eletrônico de varredura para auxiliar na melhor escolha do local a ser analisado nos cristais. O material com os grãos foi inserido em câmara com fluxo de He entre 0,35 e 0,45 1/min, posteriormente passando por um tubo de vidro contendo partículas de quartzo cobertas com ouro para a remoção de Hg²⁰⁴. Este processo minimiza a interferência isobárica com Pb²⁰⁴ e permite a aplicação das correções do Pb comum.

Após combinação com o gás de Ar, o material vaporizado foi levado até a zona do detector que consiste em 6 contadores de íons multicanal (MICs) e 4 copos de Faraday. As análises do padrão e das amostras foram obtidas por meio de sinais coletados em bloco único com 40 ciclos, cada um deles durando 1.049 s. Foi utilizada a técnica de *standard bracketing* e o padrão internacional usado foi o zircão GJ-1 fornecido pelo *ARC National Key Centre for Geochemical Evolution and Metallogeny of Continents* (GEMOC) na Austrália.

A organização e otimização dos dados foi realizada usando planilha confeccionada no Laboratório de Geocronologia da Universidade de Brasília. O tratamento dos dados geocronológicos, bem como a plotagem dos diagramas Concordia e isócronas foram realizados por meio do software ISOCHRON R (disponível em <http://pieter-vermeesch.es.ucl.ac.uk/shiny/IsoplotR>).

3.6.Microssonda Eletrônica

A análise por microssonda eletrônica permite a quantificação da composição química, bem como análise individual de minerais por meio de um feixe com menor diâmetro e maior capacidade de geração de sinal. Para que a incidência do feixe de elétrons ocorra com diâmetro controlado (variando entre 1 e 1000 µm), a microssonda eletrônica possui um feixe de elétrons colimado por uma sequência de lentes condensadoras. Conforme ocorre a interação feixe-amostra, raios-X secundários são gerados. Destes, os que possuem comprimento de onda similar ao do elemento analisado são refletidos para o detector quando atingem os cristais

analisadores (Figura 5). A partir do comprimento e da intensidade de onda que ocorre são determinados os elementos e seus teores (Goldstein *et al.*, 2003).

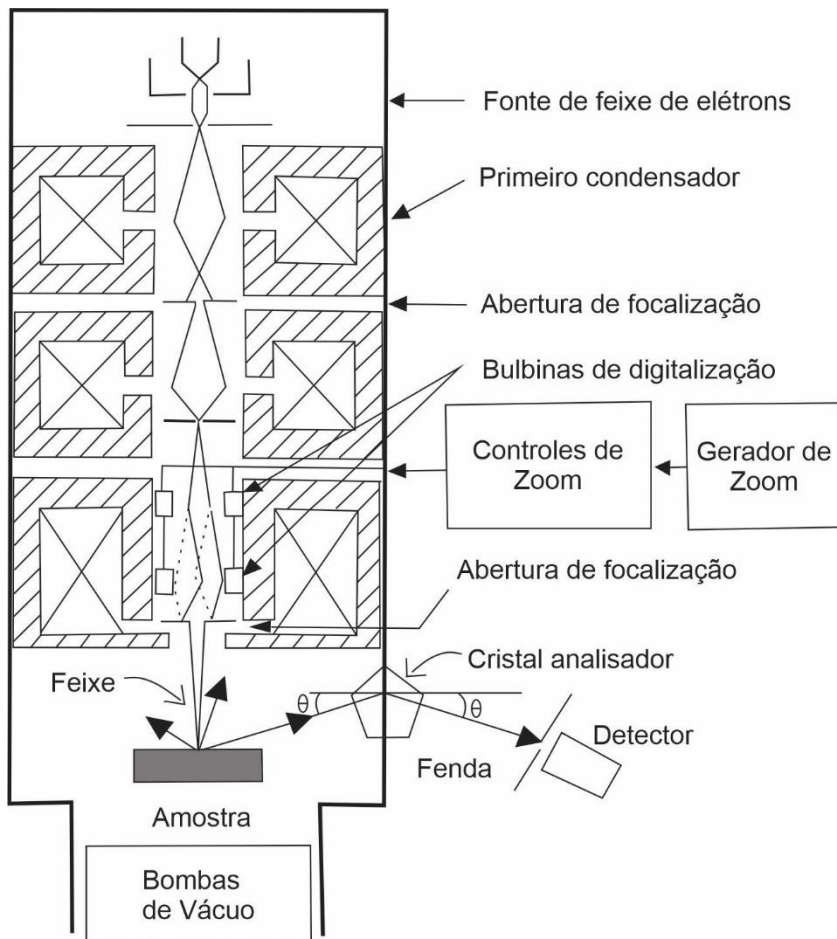


Figura 5. Ilustração esquemática de uma microssonda eletrônica, modificado de Goldstein *et al.* (2003).

Neste trabalho, as análises de microssonda eletrônica foram realizadas no Laboratório de Microssonda Eletrônica do Instituto de Geociências – UnB com um equipamento do modelo JEOL JXA-8230. O equipamento operou com voltagem entre 15 e 20 kV, corrente de 5nA e feixe com diâmetro de 1 μm e 5 μm . Foi determinada a composição química dos elementos maiores em forma de óxido que compõem os feldspatos (clastos e matriz) deformados nos plút ons Santa Terezinha e Catingueira, à sul da ZCP.

4. ARTIGO

Deformation mechanisms and zircon U-Pb geochronology of the south Patos shear zone (Borborema Province, NE Brazil)

Carolina Peixoto de Souza^{1*}, Gustavo Viegas¹

1. Instituto de Geociências, Universidade de Brasília, Brasília, DF, Brazil

ABSTRACT

The southern boundary of the Patos Shear Zone (PSZ), an important lineament of the Borborema Province, presents mylonitic rocks that record metamorphism mainly in greenschist facies. These rocks exhibit, locally, solid-state deformation evidence, suggesting an association with the transcurrent events of the PSZ. In this sector occur gneissic granitic basement, Neoproterozoic metavolcanic, and metasedimentary rocks, besides granitic and granodioritic intrusions, as the Santa Terezinha and Catingueira plutons, commonly showing stretched shapes in agreement with the main mylonitic foliation. Recrystallized quartz of these plutons accommodates the deformation by dislocation creep, under upper greenschist facies to lower amphibolite facies, while the porphyroclasts and recrystallized plagioclase and K-feldspar deform by mechanic fragmentation. The granitic gneissic host rocks show similar deformation conditions to the plutons. The OCP of the quartz crystals reveals rotational recrystallization along with the basal $\langle a \rangle$, rhomb $\langle a+c \rangle$, and prismatic $\langle a \rangle$ planes, while the feldspar occurs fractured and heterogeneous, with deformation in solid state in larger porphyroclasts. These characteristics suggest that the deformation occurred at depths equivalent to the brittle-ductile transition, marked by the coactivity of brittle and ductile mechanisms along with the intermediate crustal level. U-Pb zircon data for the Santa Terezinha pluton sample showed an age of 625 ± 7 Ma, interpreted as the age of crystallization. This data, compared to the age of 591 ± 5 Ma presented by the literature for the batholith Teixeira, which occur also in the south of the PSZ, and the age of about 565 Ma interpreted as the main metamorphic event in the PSZ, suggest different perspectives regarding the time of the deformation and magmatism events that occurred at the southern limit of this structure. The elongated shape of the Terezinha pluton in agreement with the shear zone foliation, as well as the existence of deformation in the solid-state suggest that its emplacement had an association with the PSZ transcurrent event. This

association would be possible if the interval between the generation/emplacement and magmatic crystallization of the pluton was approximately 40 Ma. Successive magmatic events may have maintained a high-temperature gradient during the pluton crystallization period, contributing to the slow cooling of the body.

Key-words: Patos Shear Zone, granitic magmatism, microstructures, geochronology, deformation mechanisms.

4.1. Introduction

The tectonic control of emplacement and exhumation of granitic bodies and its relationships with strike-slip zones have been explored and studied by several authors for more than three decades (Hutton, 1988; Vauchez and Neves, 1997; Vigneresse, 1995; Paterson and Tobisch, 1992; Rosenberg, 2004; Weinberg *et al.* 2004). In addition to the record of the final stages of the exhumation of large-scale structures, magma emplacement mechanisms play an important role in the chronological understanding of the deformational events of the orogenic system in which they are emplaced (Paterson *et al.* 1998; Brown and Solar 1998; Schmidt and Paterson, 2000; Weinberg *et al.* 2004).

Granitic plutons commonly occur parallel or slightly oblique to the main orientation of shear zones. When this relationship is established, they can be pre-, syn-or post-kinematic in relation to the structure (Hutton, 1988; Vigneresse, 1995; Vauchez *et al.* 1997). The timing of crystallization processes and subsequent shear zone deformation may be assessed mainly by the pluton shape, its internal fabrics, and its textural relationships with the host rocks (Hutton, 1988; Weinberg *et al.* 2004; Brown and Solar, 1999; Archanjo *et al.* 2002).

During the Brasiliano/Pan African orogeny (650-550 Ma) in northeast Brazil, the tectono-thermal evolution of the Borborema Province (Fig. 1) was marked by a broad and diverse granitic magmatism associated mainly with NE-SW and E-W transcurrent shear zones (Vauchez *et al.*, 1995; Vauchez *et al.*, 1997; Neves *et al.* 2000; Archanjo *et al.* 2008). Early U-Pb data for the classical types of granites of the Borborema Province established three main magmatic events in 650 - 625 Ma, 580 - 570 Ma, and 545 - 520 Ma (Van Schmus *et al.* 2011 and references therein). The characterized granitic plutons in these distinct chronological associations share the common trait of being associated with major shear zones that outcrop in

the Borborema Province, indicating feedback between magmatism and deformation in high metamorphic grade , transpressional zones (Archanjo and Bouchez, 1994; Neves *et al.* 1996; Vauchez *et al.* 1997; Archanjo *et al.* 1999; Santos and Medeiros, 1999; Neves *et al.* 2000; Brito Neves *et al.* 2003; Archanjo and Fetter, 2004; Guimarães *et al.* 2004; Neves *et al.* 2006; Archanjo *et al.* 2008; Hollanda *et al.* 2010; Viegas *et al.* 2014; Viegas *et al.* 2016).

Bordering the southern limit of the Patos shear zone, an important structure present in Borborema Province, there are medium to low- temperature mylonitic granites associated with high-temperature mylonites and metasedimentary rocks (Vauchez *et al.* 1995). Among these granitic bodies, the Catingueira and Terezinha plutons present elliptical shapes in agreement with the E-W mylonitic foliation of the shear zone, besides localized solid-state deformation, which suggests an association with the Patos Shear Zone (Vauchez *et al.* 1997).

Despite early data showing that the emplacement of both the Santa Terezinha and Catingueira plutons was late to post-kinematic (Almeida *et al.* 1967; Sial, 1986; Brito Neves *et al.* 2003, Vauchez *et al.* 1997), detailed geochronological and structural data about pluton emplacement, subsequent solid-state deformation and the relationships between these intrusions and the medium to low-temperature metamorphism of the southern boundary of the Patos shear zone are still scarce.

This contribution presents a structural study of the fabrics of the granitoid plutons, besides the host mylonites and metasedimentary rocks that outcrop in the southern sector of the Patos shear zone. The data integration of field structural mapping, microstructures, and Electron Backscatter Diffraction (EBSD) analyses of the plutons and their host rocks, we attempt to investigate the deformation mechanisms active during pluton emplacement and coeval shear deformation in the south Patos shear zone. In addition, we constrain the age of pluton emplacement within the shear zone by providing a zircon U-Pb age of the Santa Terezinha granite.

4.2.Geologic Setting

The Borborema Province (NE Brazil, Fig. 1a, b) is a wide orogenic system formed by convergent episodes between the Amazonian, São Francisco, West African, and Congo cratons during the assembly of West Gondwana (Almeida *et al.* 1981; Brito Neves *et al.* 2000; Caxito *et al.* 2020). It represents a major record of the Brasiliano orogeny (ca. 650-500 Ma), once that progressive deformation and magmatism culminated in the record of several granitoid

plutons emplaced along a complex continental scale shear zone system (Vauchez *et al.* 1995; Brito Neves *et al.* 2003; Weinberg *et al.* 2004).

The structures form a conjugate system that extends for more than 200.000 km² and present continuity along the major west African structures (Brito Neves *et al.* 2000; Caxito *et al.* 2021). Amongst them, the major E-W, dextral strike-slip faults such as the Patos and Pernambuco shear zones are attributed to the late stages of the Brasiliano orogeny and were proxies to define the Northern, Central and Southern geotectonic domains of the Borborema Province (Fig.1b; Van Schmus *et al.* 1995; 2008).

The Patos shear zone (Fig. 1b, c) extends for approximately 600 km in the E-W direction and divide the Northern and Central tecnotic domains (Fig. 1). This shear zone is characterized as a transpressional and mainly dextral structure, presenting high temperature, amphibolite-facies mylonites in the northern and central portions that are variably affected by partial melting (Corsini *et al.* 1991, Viegas *et al.* 2014). The best estimate for the peak metamorphic conditions is around 566 ± 6 Ma, obtained through the U-Pb SHRIMP method in zircon in a leucogranite with transitional contacts with host diatexites (Viegas *et al.* 2014).

The southern boundary of the shear zone is marked by the intrusion of granitoid bodies defined as the Catingueira and Santa Terezinha plutons, which occur parallel to slightly oblique to the E-W direction of the structure. These rocks have elongated shapes, are approximately 1 km wide and 10 km long, and crosscut the metasedimentary and metavolcanic rocks of the Cachoeirinha-Salgueiro belt (Vauchez *et al.*, 1997; Brito Neves *et al.* 2000; Van Schmus *et al.* 2011). Solid-state deformation is locally observed in these granitoids, which suggests that the intrusions are partially affected by the Patos shear zone (Vauchez *et al.* 1997).

The study area is situated in the southern boundary of the Patos Shear Zone (Fig.1c), which is composed of granitic to gneissic basement rocks, Neoproterozoic metasedimentary and metavolcanic rocks, as well as intrusive granites and granodiorites (Corsini *et al.* 1991; Archanjo *et al.* 2008; Viegas *et al.* 2014). The related medium- to low-temperature mylonites and ultramylonites rework the high-temperature mylonites and migmatites of the northern segment of the Patos Shear Zone (Vauchez *et al.* 1995; Viegas *et al.* 2014).

Early studies have suggested that the emplacement of both the Santa Terezinha and Catingueira plutons was late to post-kinematic in relation to the Patos shear zone (Almeida *et al* 1967; Sial, 1986; Brito Neves *et al* 2003, Vauchez *et al*, 1997). Brito Neves *et al.* (2003) presented an age of 573 ± 45 Ma to the Catingueira pluton. The data was obtained through the

zircon U/Pb method in a homogeneous leucocratic syenogranite, located in a quarry close to Catingueira town. At the same place, the authors showed Sm/Nd data with $T_{DM}=2397$ Ma age, and $\varepsilon_{Nd600}=-15,65$, suggesting Paleoproterozoic sources.

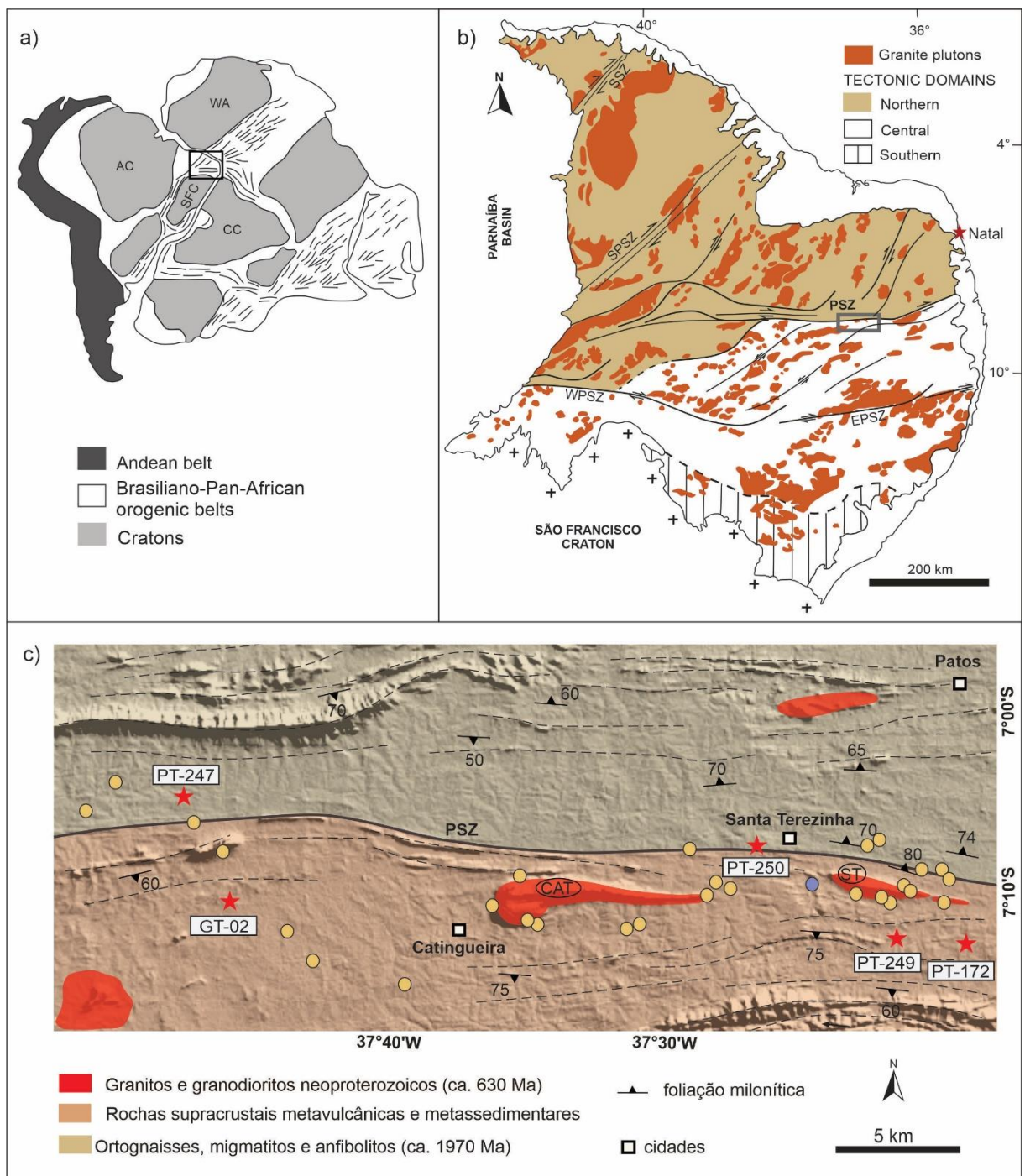


Figure 1 a) Reconstruction of South-America-Africa exhibiting the Amazonian, São Francisco, West African, and Central Congo Cratons, Brasiliano-Pan-African belts, and Andean Belt. The black square represents the Borborema Province; (b) Schematic map displaying the tectonic domains of Borborema Province (northern, central, and southern) and the main shear zones: SSZ (Sobral Shear Zone); SPSZ (Senador Pompeu Shear Zone); PSZ (Patos Shear Zone); WPSZ (West Pernambuco Shear Zone), and EPSZ (East Pernambuco Shear Zone). The gray square represents the study area; (c) Schematic geological map of the southern Patos Shear Zone, displaying the Paleoproterozoic orthogneisses, migmatites, and amphibolites of the basement, the supracrustal rocks, and Neoproterozoic granites and granodiorites (CAT-Catingueira pluton, ST-Santa Terezinha pluton). The main trend of the mylonitic foliation, mineral stretching lineations, locations of field mapping points (yellow dots), geochronological (blue dot), and EBSD analysis (red stars) samples are shown; (d) Mesoscale structural fabrics (foliation; n=25) and the mineral stretching lineation (n=15) the central-south PSZ. Modified from Neves et al. 2003; Hollanda et al. 2010; Archanjo et al. 2008; Viegas et al. 2014; Castellan et al. 2020.

4.3. Methods

4.3.1. Field structural mapping

The field structural analysis was performed through orthogonal profiles across the main E-W length of the shear zone. Collected field data included geometric relationships between main structures and kinematic criteria in different sectors of the shear zone. Main investigated structural features of the outcrops, such as deformation intensity, mineral textures, and mesoscopic identification of clasts and fine-grained matrix, were documented. In all outcrops visited, representative samples were collected and oriented according to their foliation and lineation patterns.

4.3.2. Microstructures and EBSD analysis

A total of twenty-three oriented and polished thin sections were cut in the XZ plane of the structural reference frame, perpendicular to the foliation (Z) and parallel to the lineation (X). Deformation microstructures and petrographic aspects were studied via polarized light and electron microscopy at the Microscopy Laboratory of the University of Brasília, Brazil. The crystallographic fabrics of recrystallized quartz grains were studied via electron backscatter diffraction (EBSD) analysis of representative samples collected along the southern border of the shear zone (location in Fig. 1c).

In order to ensure a clear surface of the samples, a chemo-mechanical polishing using colloidal silica was applied for ~2-3 hours. The polished thin sections were carbon-coated

for analysis under high-vacuum conditions and uncoated in a low-vacuum environment. EBSD analysis of characteristic areas of the deformed/recrystallized microstructure were performed with a JEOL JSM 5600 scanning electron microscope (SEM) equipped with an Oxford Instruments/HKL Nordlys EBSD detector at *Géosciences Montpellier*. Data acquisition was obtained with the Channel5 software (Oxford Instruments), and analytical conditions were of 75° sample tilt, working distance of 25 mm, and 17 kV accelerating voltage. Step sizes ranged from 0.5 to 4 µm depending on microstructural heterogeneity.

Treatment of EBSD data was performed with the MTEX version 5.0.3 toolbox for MATLAB (Hielscher and Schaeben, 2008), which was used to generate pole figures, misorientation axes, and misorientation angle distributions. Pole figures were plotted as contoured diagrams in which the average orientation of the grains is represented as one point per grain density. The contouring of the crystallographic axes of quartz grains was constructed based on multiples of uniform distribution (M.U.D.) and represented in a standard grayscale.

4.3.3. *Mineral chemistry*

The chemical composition of feldspars (porphyroclasts and recrystallized grains) in the granitoids was measured using a Jeol JXA 8230 Electron Probe Micro Analyzer at the Electron Micropobe Laboratory, University of Brasília. The analysis was obtained with accelerating voltage of 15-20 kV, current of 5 nA, and beam diameter of 1 µm for K-feldspar and 5 µm for plagioclase.

4.3.3.1. *Zircon U-Pb geochronology*

A sample of the Santa Terezinha pluton from the south Patos Shear Zone (PUR-02D) was selected for zircon U-Pb age dating at Geochronology Laboratory, University of Brasilia. The sample was initially crushed and sieved, and then the heavy minerals were separated using conventional gravimetric and magnetic methods. Zircon grains were then handpicked using a binocular microscope, mounted on the epoxy resin (0.5 cm), and polished (1 µm) for Laser Ablation Inductively Coupled Plasma Mass Spectrometry (LA-MC-ICP-MS) isotope ratio acquisition.

Back-scattered images of analyzed zircon crystals were acquired in a FEI QUANTA 450 scanning electron microscope (SEM) at the Electron Microscopy Laboratory,

University of Brasília. Analytical conditions were of 10 nA beam current, 20kV accelerating voltage, and 13.8 mm working distance. The laser ablation system is ESI/New Wave Research, UP-213, Nd: YAG, with low volume cell (ca. 4 cm³). The laser wavelength is 213 nm, with 3ns pulse width, fluence from 3.0 to 3.5 J cm⁻², repetition rate 10 Hz, spot size 25 µm, and carrier gas of 100% He, Ar make-up gas combined using a Y-piece along the sample transport line close to the torch.

The duration of pre-ablation laser warm-up is about 10 s, the ablation duration is 40 s, the wash-out delay 20 s, ablation pit depth have ~10 µm, and the cell carrier gas flow 0.40 l min⁻¹ He. Isotopic analyses were performed on a Thermo-Fischer, Neptune, MC-ICP-MS, ablation aerosol, 1050 W, 0.997 l min⁻¹ sample gas flow, mixed Faraday cups, and multiple ions counting (MIC) array. The masses measured were Faraday ²³²Th, ²³⁸U, and ²⁰⁶Pb, and MIC ²⁰²Hg, ²⁰⁴Pb, ²⁰⁷Pb, and ²⁰⁸Pb, with a total integration time per output data point of 1.049 s. Normalization was performed with GJ1 (Jackson *et al.* 2004, Horstwood *et al.* 2016) as the primary reference material and the 91500 (Wiedenbeck *et al.* 1995) is used as a secondary validation.

The data processing package used is lolite v. 4. 0 (Paton *et al.*, 2011) & VizualAge (Petrus and Kamber, 2012), using exponential plus linear modeling for LIEF correction. The quality control is about 91500 – Conc age = 1063 ± 3 (2s, MSWD_{c+e} = 0.27, n = 16) and the systematic uncertainty for propagation is 1% (2s). The age calculations were performed using in-house developed Excel spreadsheets and all U–Pb plots were created using the Isoplot software (Ludwig, 1993).

4.4. Results

4.4.1. Field and petrographic observations

The southern Patos Shear Zone comprises gneissic granites, metavolcanic and metasedimentary rocks that are intruded by granitic plutons (Fig. 1c). The rocks commonly exhibit an E-W-trending mylonitic foliation marked by millimeter to centimeter-scale elongated quartz ribbons and stretched K-feldspar porphyroclasts.

The granitic gneiss are composed by K-feldspar (30%), plagioclase (25%), quartz (20%), and biotite (10%), and display fine to coarse-grained mafic and felsic parallel bands (Fig. 2a). The mafic bands show elongated biotite crystals, in addition to rounded quartz grains,

and stretched feldspars, both with millimeter sizes (Fig. 2b). The felsic bands comprise centimeter-scale quartz crystals and elongated porphyroclasts of K-feldspar that are fractured and have *augen*-shaped morphologies (Fig. 2b,c). The contact between the bands is abrupt and, locally transected by oblique fractures. Quartz veins are parallel to the mylonitic foliation (Fig. 2b).

Muscovite-bearing metasedimentary rocks occur interspersed with the gneissic granites. They present a light grey to brown color and have a silky textural aspect. Quartz, biotite, muscovite, and K-feldspar are the main mesoscopic mineral phases. In some portions, a porphyroclastic texture is observed, defined by elongated and fractured K-feldspar porphyroclasts that are immersed in a polymimetic, fine-grained matrix. A gradual transition from mylonitic to ultramylonitic fabric is observed mainly as: i) increase in the matrix percentage and distribution, ii) progressive decrease in grain size coupled with gradual absence of porphyroclasts, iii) preferred orientation of biotite and muscovite lamellae, and iv) stretching of K-feldspar clasts.

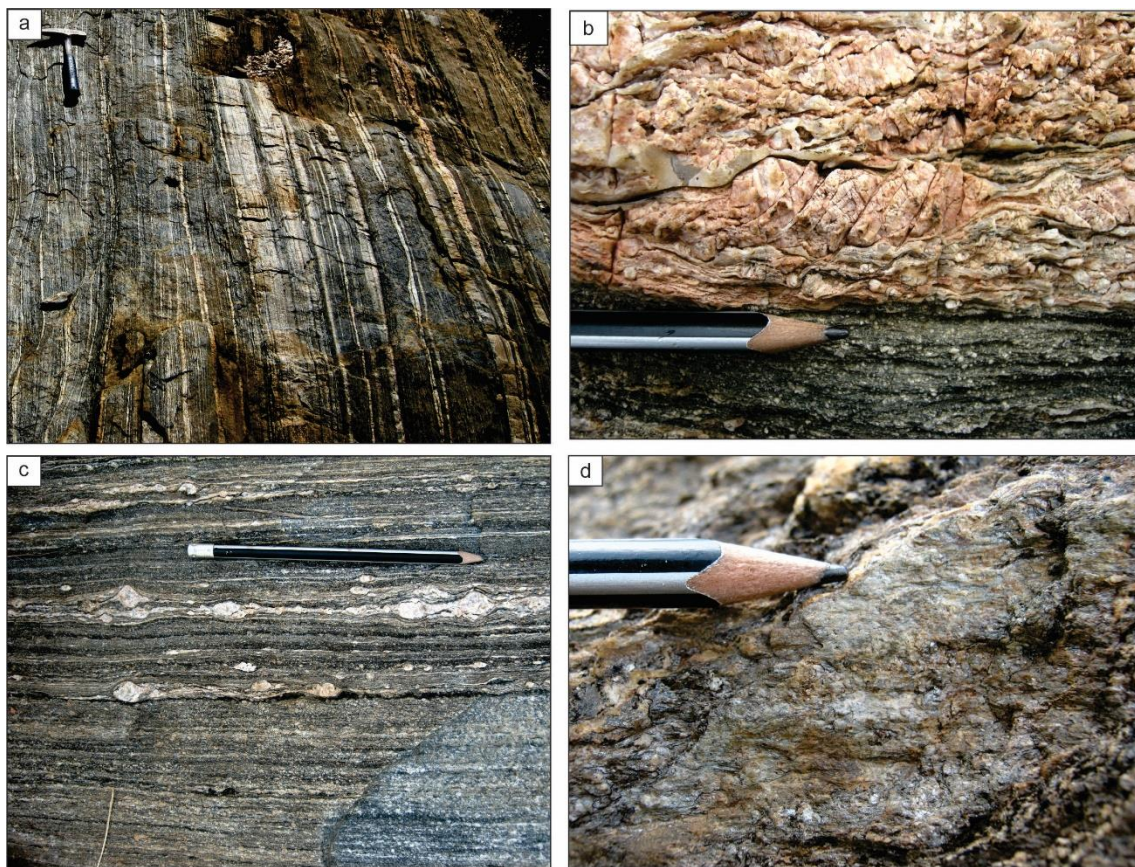


Figure 2. Field aspects of the mylonites and ultramylonites from the southern boundary of the Patos shear zone. (a) Granitic gneiss showing fine to coarse-grained mafic and felsic bands, both parallel to the E-W mylonitic foliation of the Patos shear zone. (b) Contact between the mafic and felsic bands of the gneissic granite. The mafic band shows millimetric biotite crystals aligned to the mylonitic foliation, in addition to rounded quartz grains and elongated feldspars. The felsic band presents centimeter-scale porphyroclasts of K-feldspar that are elongated and fractured. A quartz vein parallel to the mylonitic foliation is observed close to the K-feldspar porphyroblast. (c) Fine-grained mafic and felsic bands of the gneissic granite. The felsic bands display K-feldspar porphyroclasts elongated and with augen shapes. (d) Muscovite-rich metapelites. The mylonitic foliation is marked by elongated muscovite and biotite that are aligned with subordinate, stretched K-feldspar porphyroclasts.

The Santa Terezinha pluton occurs in the southern boundary of the Patos Shear Zone (Fig.1) and is characterized by a 5 km length, elongated body that is concordant with the WNW-ESE trend of the structure (Fig. 1c). It is composed of quartz (30%), K-feldspar (25%), plagioclase (20%), biotite (~7%), and muscovite (~5%). The granite color ranges from light to medium grey, and a porphyroclastic texture is widespread (Fig. 3a,b). The centimetric K-feldspar porphyroclasts are elongated, locally *augen*-shaped, and wrapped by millimeter-scale stretched biotite crystals (Fig. 3b).

The Catingueira pluton is characterized by an E-W, elongated *en-cornue* intrusion with dimensions of 600 m in width and 12 km in length, parallel to the main trend of the Patos shear zone (Fig.1c). The main mineral assemblage comprises K-feldspar (35%), plagioclase (30%), quartz (20%), and biotite (~10%). The granitic body has a light grey color, an equigranular texture, and an incipient foliation that is evidenced by the preferred orientation of millimeter-scale biotite lamellae (Fig. 3c). Ultramylonitic bands occur locally and are composed of fine-grained biotite and quartz crystals, as well as millimetric to centimetric quartz veins (Fig. 3d).

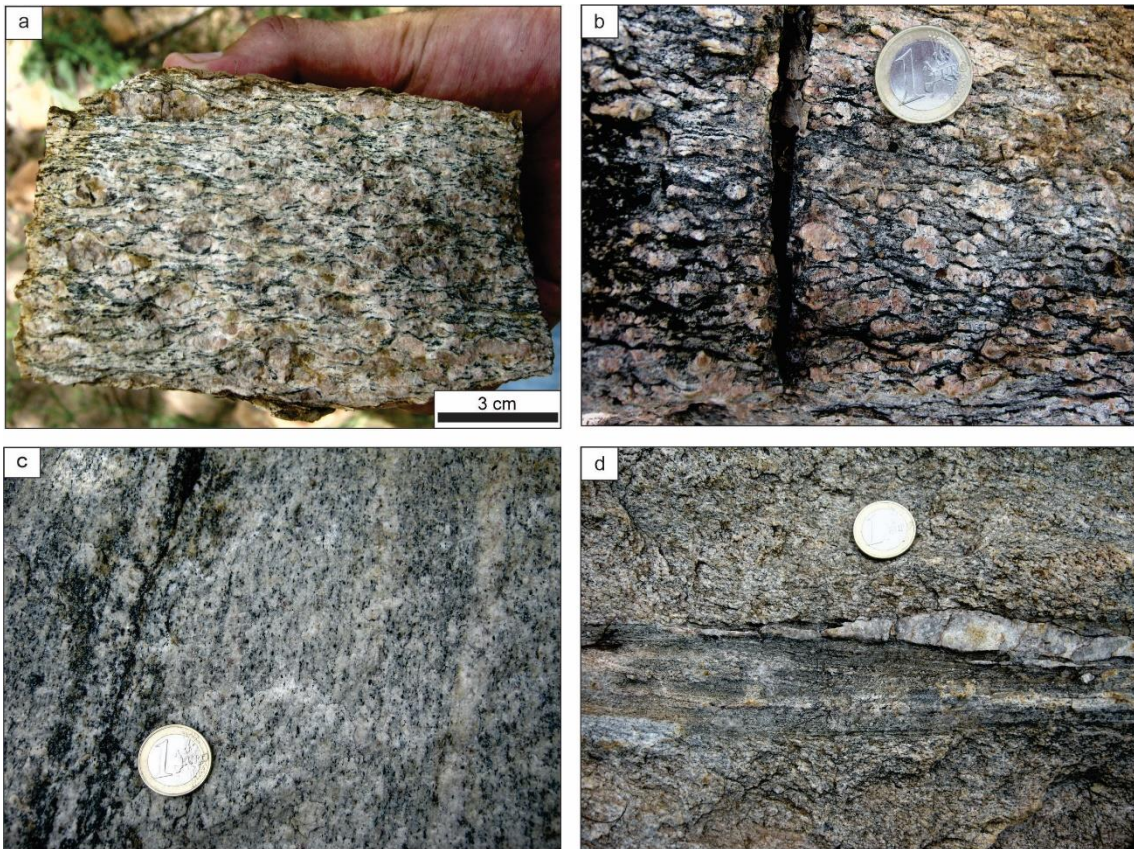


Figure 3. Field aspects of the Santa Terezinha and Catingueira plutons: (a) Santa Terezinha pluton showing a porphyroclastic texture marked by elongated K-feldspar porphyroclasts. The stretched K-feldspar clasts, elongated quartz ribbons and biotite crystals mark the mylonitic foliation. (b) Santa Terezinha pluton presenting centimeter K-feldspar porphyroclasts elongated and developing *augen* morphologies. The porphyroclasts are wrapped by millimeter-scale biotite crystals aligned with the mylonitic foliation. (c) Catingueira pluton showing a light grey color, fine-grained equigranular texture, and an incipient foliation that is evidenced by the preferred orientation of millimetric biotite crystals. (d) Ultramylonite band in Catingueira pluton exhibiting fine-grained biotite and a centimetric quartz vein parallel to the mylonitic foliation.

4.4.2. Microstructure

4.4.2.1. Granitic Gneiss

The granitic gneiss are characterized by porphyroclasts of K-feldspar and plagioclase ($500 \mu\text{m} - 3, 5 \text{ mm}$) wrapped by quartz ribbons ($50 \text{ to } 200 \mu\text{m}$) and a fine-grained recrystallized matrix ($30 - 50 \mu\text{m}$) mostly composed by quartz + feldspar + biotite (Fig. 4a).

The porphyroclasts of K-feldspar and plagioclase have sizes ranging from $500 \mu\text{m}$ to $3,5 \text{ mm}$ (Fig. 4). They display sub-elliptical to rounded shapes and lobate boundaries (Fig.

4c, d, e, f). Some clasts display recrystallized, strain-free grains at their boundaries; these grains have around 150 μm , anhedral shape, and lobate boundaries (Fig. 4e). The clasts exhibit perthitic texture, undulose extinction and deformation twins (Fig. 4c, f). Microfractures commonly crosscut the clasts forming angular fragments ($\pm 800 \mu\text{m}$; Fig. 4f) and record offsets of up to 50 μm (Fig. 4c, d, f). Locally, the microfractures are asymmetrical and indicate a sinistral shear sense (Fig. 4d).

Quartz crystals occur as polycrystalline ribbons with aspect ratios varying from 1:10 to 1:20 (Fig. 4a, b, d). The grains have sizes ranging from 50 to 200 μm with lobate boundaries and undulose extinction (Fig. 4b, d). The contact of quartz ribbons with the surrounding grains is mainly straight and they occur parallel to the ESE-WNW trending mylonitic foliation (Fig. 4a, b, d).

The recrystallized matrix comprises quartz ($\pm 30 \mu\text{m}$), feldspar ($\pm 30 \mu\text{m}$), and biotite ($\pm 50 \mu\text{m}$) grains (Fig. 4b, c, e, f). Feldspar displays rounded shapes and lobate boundaries. Quartz crystals occur with rounded to polygonal shapes and lobate to straight boundaries. The biotite grains have elongated shapes and are subparallel to the mylonitic foliation (Fig. 4b).

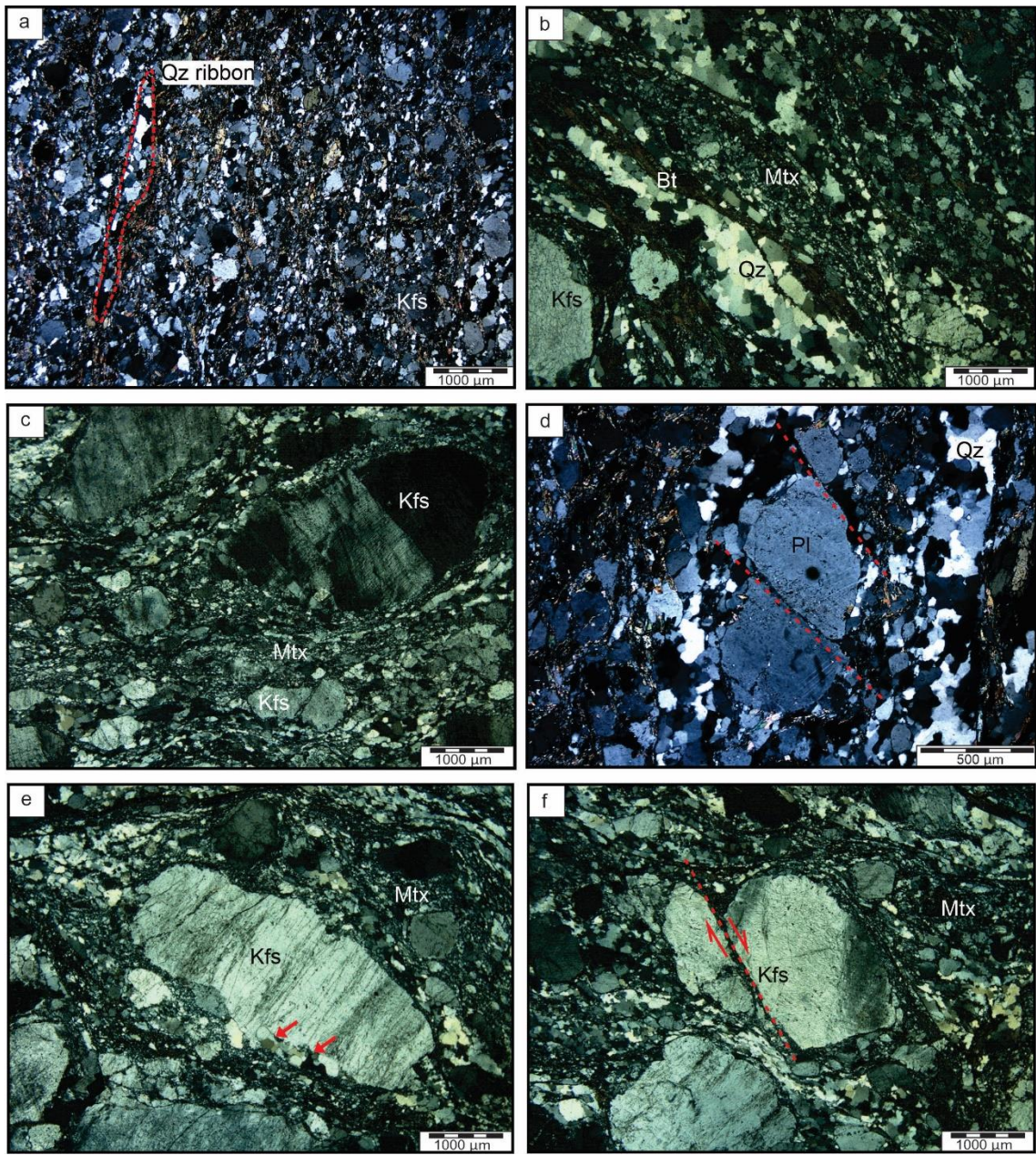


Figure 4. Microstructures of the mylonitic gneisses of the southern Patos shear zone (Qz = quartz, Kfs = K-feldspar, Pl = plagioclase, Bt = biotite, Mtx = matrix; Whitney and Evans, 2010) (a), (b) Overview of typical mylonitic granite with porphyroclasts of K-feldspar and plagioclase wrapped by quartz ribbons and fine-grained recrystallized K-feldspar, plagioclase, quartz and biotite. The mylonitic foliation is defined by the preferred orientation of quartz ribbons, elongated feldspar clasts, and oriented biotite; c), d) Sub-elliptical K-feldspar and plagioclase porphyroblast embedded in the fine-grained recrystallized matrix and showing undulose extinction. A

sinistral shear sense defined by asymmetric displacement along oblique microfractures is locally observed in plagioclase clasts [d]; e) Recrystallized grains rimming a K-feldspar clast. The grains are strain-free and have lobate boundaries; f) Rounded and fractured K-feldspar porphyroblast with weak undulose extinction. The fracture crosscuts the clast and originates angular fragments.

4.4.2.2. Santa Terezinha Pluton

This pluton is characterized by the development of porphyroclastic mylonites that display porphyroclasts of feldspar ($700 \mu\text{m} - 2,5 \mu\text{m}$) wrapped by quartz ribbons ($\pm 150 \mu\text{m}$) that are embedded in a fine-grained ($\pm 20 \mu\text{m}$), recrystallized polyphase mixture (quartz + feldspar + biotite; Fig. 5a).

The porphyroclasts are mainly K-feldspar and plagioclase with grain sizes ranging between $700 \mu\text{m}$ to 2.5 mm (Fig. 5a, c, d, e, f). The clasts are sub-elliptical, locally rounded (Fig. 5a), with *augen*-shaped geometries and aspect ratios around 1:3 (Fig. 5 c, d, e, f). They display irregular, lobate subgrain boundaries as well as a weakly developed undulose extinction. Perthites, mechanical twins, and myrmekite are observed in some of the K-feldspar and plagioclase clasts. Intragranular and transgranular microfractures show a mean thickness of $30 \mu\text{m}$ (Fig. 5c-d-e-f). Most of these cracks are filled by the fine-grained, recrystallized matrix ($\pm 15 \mu\text{m}$; Fig. 5c, e, f), and locally by quartz fragments ($\pm 50 \mu\text{m}$; Fig. 5d).

The intragranular microfractures are straight and can be filled with fragments ($\pm 100 \mu\text{m}$) of the host clast with irregular shapes and variable sizes. They display kinematic offsets up to $100 \mu\text{m}$ and may result in rotated, bookshelf-like structures with dextral shear sense (Fig. 5c). Some clasts display recrystallized asymmetric tails composed of feldspar grains ($\pm 10 \mu\text{m}$), quartz crystals ($\pm 25 \mu\text{m}$) and grains of the polyphase mixture (quartz + feldspars + biotite; $\pm 10 \mu\text{m}$; Fig. 5e).

Quartz occurs mainly as polycrystalline ribbons with aspect ratios varying from 50:1 to 10:1 (Fig. 5b, c, f). The mean grain size is $150 \mu\text{m}$. The crystals have polygonal to irregular shapes and straight boundaries that define triple junctions (Fig. 5b). Typical substructures are undulose extinction and subgrain boundaries (Fig. 5b). The subgrains have $\pm 50 \mu\text{m}$ and straight to curved boundaries.

The recrystallized matrix is composed of fine-grained plagioclase ($\pm 20 \mu\text{m}$), K-feldspar ($\pm 20 \mu\text{m}$), quartz ($\pm 15 \mu\text{m}$), and biotite ($\pm 10 \mu\text{m}$; Fig. 5a, e, f). Feldspar grains display slightly rounded shapes, lobate boundaries, and weak undulose extinction. Quartz has irregular

shapes and lobate to straight boundaries, whilst biotite crystals are elongated and parallel to the mylonitic foliation.

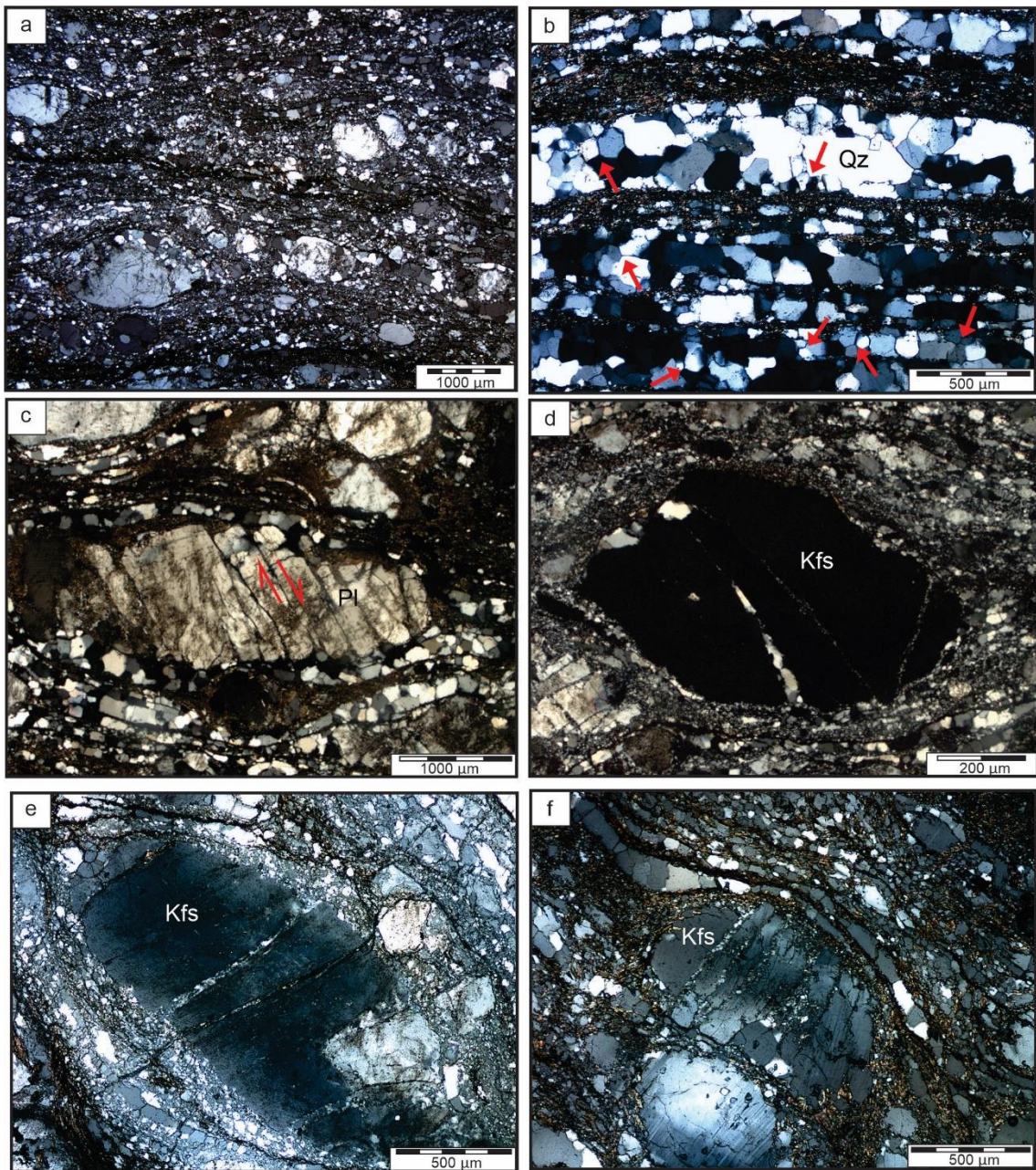


Figure 5. Microstructures of the Santa Teresinha pluton (Pl = plagioclase, Kfs = K-feldspar, Qz = quartz; Whitney and Evans, 2010). (a) Porphyroclasts of feldspar embedded in a fine-grained polyphasic matrix (quartz + feldspar + biotite). Quartz ribbons locally wrap around the clasts; (b) Foliation-parallel quartz ribbons with undulose extinction and straight boundaries that define triple junctions (red arrows); (c) Bookshelf fracturing pattern with dextral shear sense of microfracture set (red arrows) in plagioclase porphyroblast; (d) Augen-shaped K-feldspar porphyroblast displaying intragranular microfracture filled by quartz grains; e), f) Sub-elliptical K-feldspar porphyroclasts displaying microfractures filled by the fine-grained matrix (quartz + feldspars), and surrounded by quartz ribbons and the recrystallized matrix (quartz + feldspars + biotite).

4.4.2.3. Catingueira pluton

The microstructure of the Catingueira protomylonitic monzogranite comprises feldspar porphyroclasts (500 – 2000 µm) that are wrapped by quartz ribbons (\pm 270 µm) and immersed in a fine-grained, quartz-feldspathic matrix (\pm 50 µm; Fig. 6a, b, c).

Feldspars porphyroclasts are typically sub-elliptical to rounded, have straight boundaries and grain sizes of 500 µm to 2 mm (Fig. 6a, b, c). Microstructures are characterized by weak undulose extinction and deformation twins (Fig. 6a, b). Discontinuous intragranular microfractures are observed in the clasts and some of them are filled by elongated quartz crystals (\pm 50 µm; Fig. 6a). Locally, some of these fractures are rotated in a bookshelf-like structure.

Quartz ribbons have grain sizes around 270 µm, polygonal to irregular shapes and straight boundaries that define triple junctions with other phases (Fig. 6c, d). Locally, subgrain boundaries occur with grain sizes around 50 µm and lobate boundaries (Fig. 6c, d). The quartz crystals are also observed as coarse-grained polycrystalline aggregates with a mean grain size of 200 µm (Fig. 6a, b).

Amphibole crystals are partially altered to biotite and have sizes ranging from 500 µm to 1 mm (Fig. 6b, d). They have an elongated shape, straight to irregular boundaries and are parallel to the mylonitic foliation (Fig. 6b, d).

The fine-grained matrix comprises mainly recrystallized quartz and feldspar grains with a mean grain size of 30 µm (Fig. 6a, b). Both show lobate grain boundaries, with quartz grains locally displaying straight boundaries.

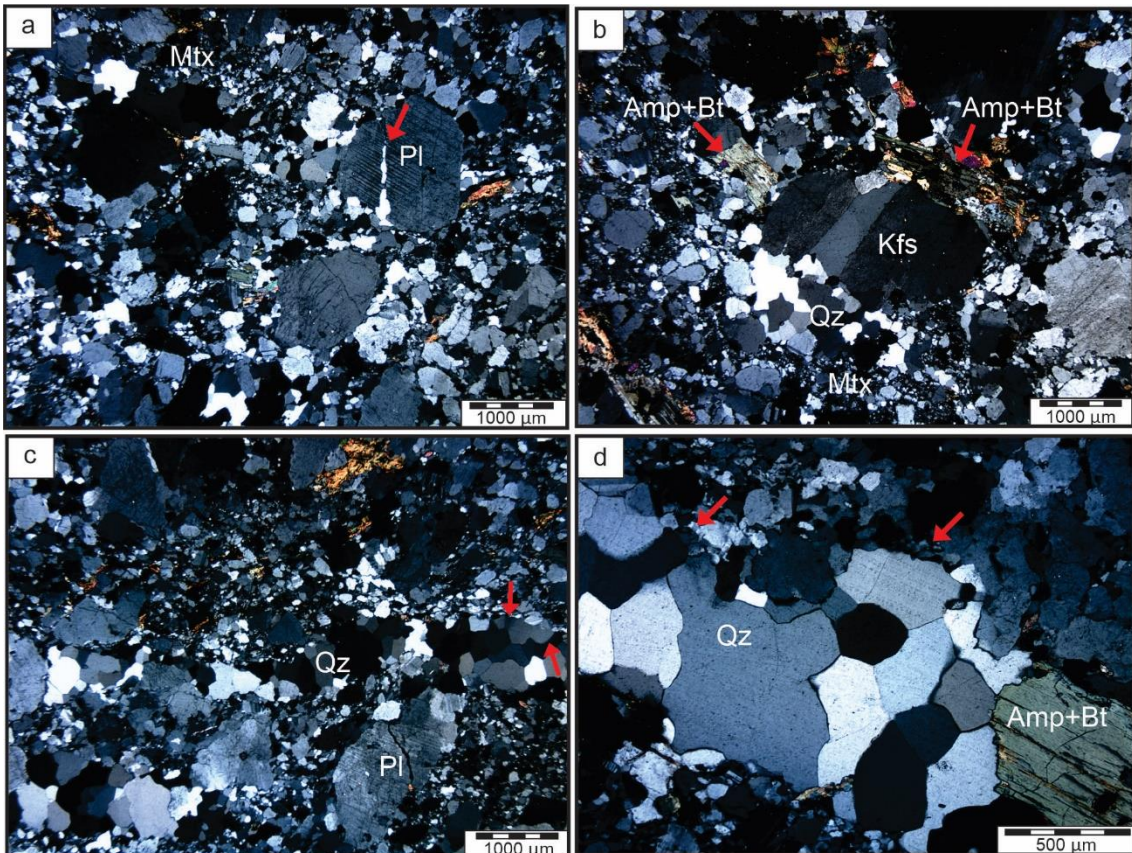


Figure 6. Microstructures of the Catingueira pluton (Qz = quartz, Pl = plagioclase, Kfs = K-feldspar, Amp = amphibole, Bt = biotite, Mtx = fine-grained matrix; Whitney and Evans, 2010). (a) Plagioclase porphyroblast showing a microfracture filled with quartz grains (red arrows) and weak deformation twins. (b) K-feldspar clast with undulose extinction wrapped by coarse-grained polycrystalline quartz aggregates and amphibole crystals changing to biotite (red arrows) parallel to the mylonitic foliation. (c) Quartz ribbons wrapping around plagioclase porphyroclasts. Subgrain boundaries in quartz ribbons are indicated by red arrows. (d) Quartz ribbon displaying straight boundaries and polygonal shapes that define triple junctions. Subgrain boundaries are indicated by red arrows. Amphibole occurs as grains parallel to the ribbon elongation.

4.4.3. EBSD analysis of quartz CPO in the host mylonites

Quartz crystallographic fabrics of mylonites located at the southern boundary of the Patos shear zone are marked by two main patterns: i) small maxima of the c-axis at the periphery of the diagram, close to Z (PT172, 247, Fig. 7a, d), and maxima located at the center of the pole figure, in Y (PT249, 250, GPT2, Fig. 7b, c, e). The scattered distribution of orientations in

samples that have maxima close to Z may define asymmetrical girdles that are consistent with the dextral shear sense of the shear zone (e.g. PT 247, Fig. 7d).

Misorientation axes for subgrains (2-10°) and high angle grain boundaries (10-45°) show maxima parallel to the [c]-axis for all samples, with a limited degree of dispersion of high angle boundaries in samples that have a weaker CPO (e.g. PT172, GPT2, Fig. 7a, e).

Correlated misorientation angle distributions show high-frequencies of low-angle misorientations for all samples, with peaks at angles between 5 and 10° (Fig. 7a-e). Uncorrelated distributions deviate from the theoretical random curve in samples that have strong CPO (PT249, 250); these are accompanied by high frequency peaks of correlated distributions at angles of 40-60° (Fig. 7c).

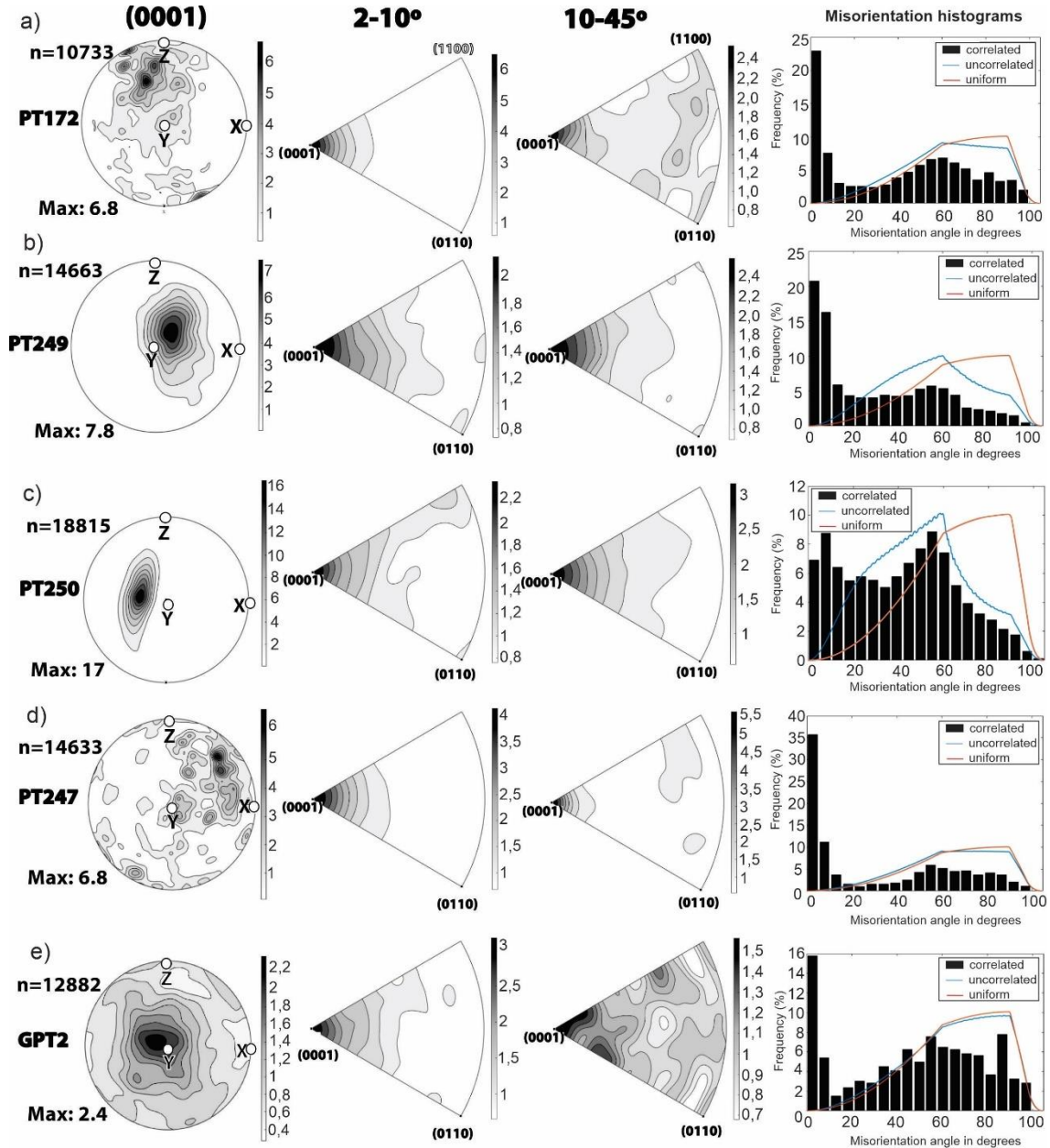


Figure 7. EBSD results for the mylonitic fabrics of the southern boundary of Patos shear zone, illustrating pole figures, misorientation axes for low- ($2-10^\circ$) and high angle ($10-45^\circ$) boundaries, and misorientation angle distributions. See text for discussion.

4.4.4. Mineral Chemistry

K-feldspar porphyroclasts of the Santa Terezinha Pluton presents a variation in Or_{88-96} contents and An values close to zero (Fig. 8a). The high Or values indicate that these feldspars are K-sanidine (Fig. 9a). The matrix shows Or values ranging between 93 and 94, with a major concentration in the core, being also classified as K-sanidine (Fig. 9a). Plagioclase have An contents that show little variation (An₁₇₋₂₀), with two samples showing lower values

(Fig. 8b; An_{13.3} and An_{15.8}). The matrix-rim plagioclase analyses have An values of An_{18.3} and An_{19.8}, and two matrix-core plagioclase samples present An_{18.1} and An_{21.80}. Most plagioclase samples show small Or contents, with one porphyroblast sample showing Or_{2.5} (Fig. 8b). The plagioclase porphyroclasts and matrix are classified in the feldspar diagram as oligoclase (Fig. 9a).

The Catingueira pluton shows a compositional variation between porphyroclasts and recrystallized matrix of the plagioclase samples marked mainly by a decrease of An contents in the recrystallized mixture (Fig. 8d). The plagioclase porphyroclasts present An₁₈₋₂₀ and the Or content varies from 0.5 to 2.4 (Fig. 8c). In contrast, plagioclase grains in the matrix are marked by a decrease in An content (An₁₈₋₁₅) and similar Or contents with the porphyroclasts (0.9 and 1.6; Fig. 8d). The porphyroclasts and recrystallized grains of plagioclase are classified in the feldspar diagram as oligoclase (Fig. 9b). K-feldspar porphyroclasts show Or₈₀₋₁₀₀ and are classified as K-sanidine (Fig. 8c, 9b).

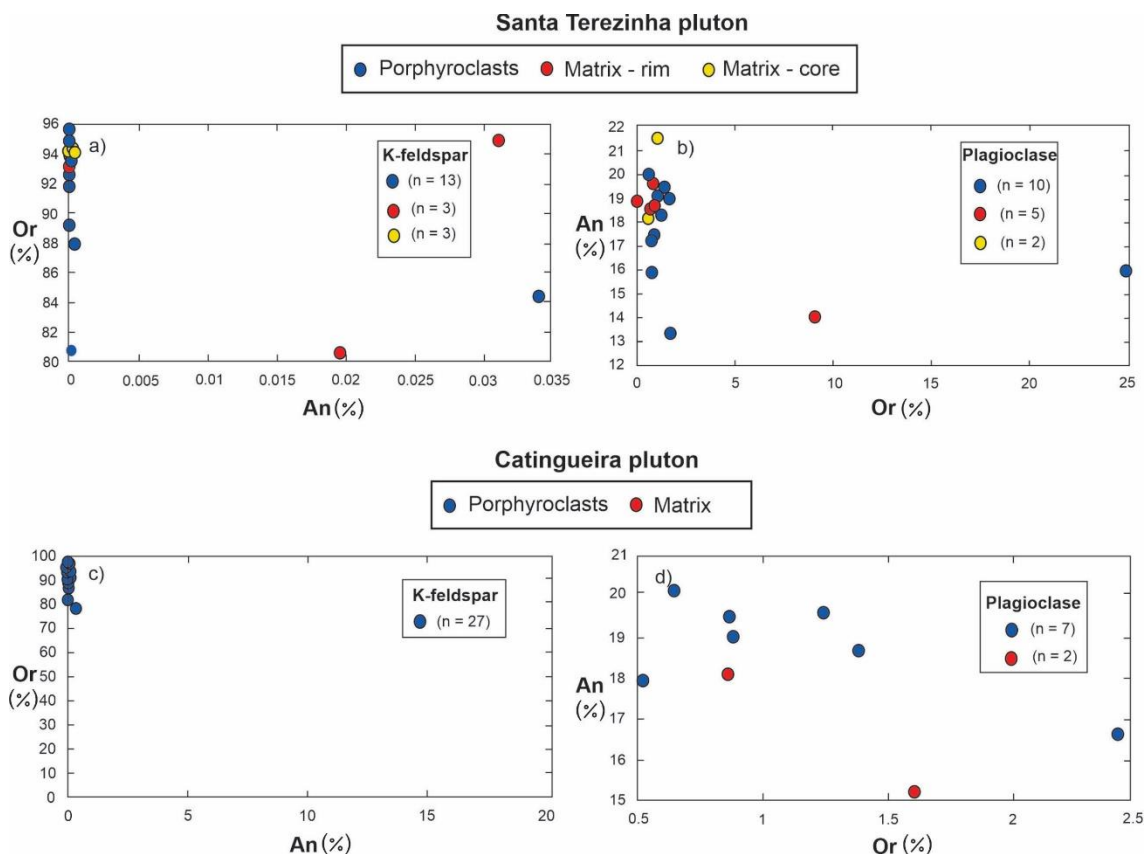


Figure 8. Chemical composition of K-feldspar and plagioclase porphyroclasts and recrystallized matrix:
(a,b) Santa Terezinha pluton (c,d) Catingueira pluton.

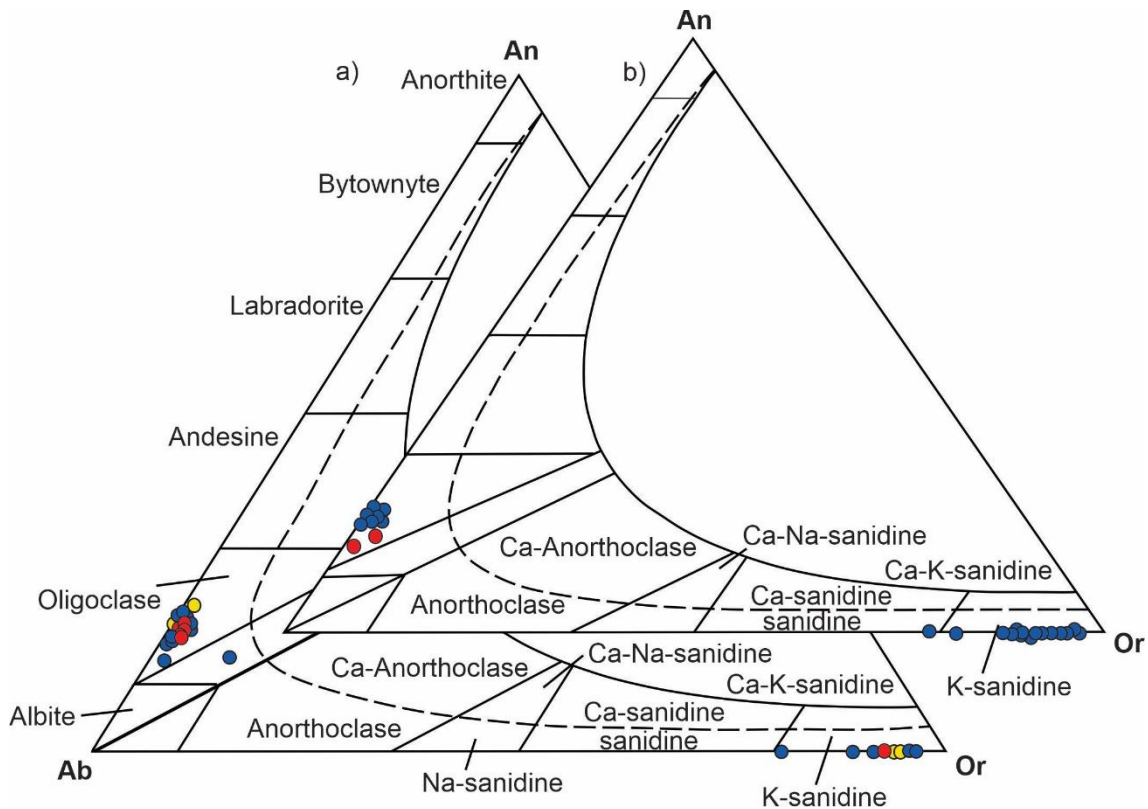


Figure 9. Feldspar classification diagrams for the (a) Santa Terezinha pluton and (b) Catingueira pluton.

Table 1. Representative major element chemical analyses for the Santa Terezinha pluton. Table of average of the obtained values.

	PUR-02					
	K-feldspar			Plagioclase		
Bulk Composition (XRF)	Porphyroclasts	Recrystallized	Porphyroclasts	Recrystallized	Core	Rim
SiO ₂	60.08	64.982	62.756	62.523	63.563	63.267
TiO ₂	79.87	0.004	0.013	b.d.l	b.d.l	b.d.l
Al ₂ O ₃	101.96	19.621	19.697	19.818	22.887	22.423
FeO	71.84	0.034	0.089	0.114	b.d.l	0.128
MnO	70.94	0.029	0.012	0.006	0.023	b.d.l
MgO	40.3	b.d.l	b.d.l	b.d.l	b.d.l	0.003
CaO	56.08	b.d.l	b.d.l	b.d.l	4.033	3.999
Na ₂ O	61.98	0.532	0.722	0.764	9.057	9.108
K ₂ O	94.2	14.64	15.418	15.553	0.247	0.13
Cr ₂ O ₃	151.99	b.d.l	b.d.l	0.015	0.027	0.036
NiO	74.69	b.d.l	b.d.l	b.d.l	b.d.l	b.d.l

Total	99.842	98.746	98.792	99.837	99.091	99.977
OH	b.d.l	b.d.l	b.d.l	b.d.l	b.d.l	b.d.l
Si	3.012	2.928	2.913	2.818	2.826	2.809
Ti	b.d.l	0.001	b.d.l	b.d.l	b.d.l	0.001
Al	1.072	1.083	1.088	1.196	1.18	1.177
Cr	b.d.l	b.d.l	0.001	0.001	0.001	b.d.l
Fe	0.001	0.003	0.004	b.d.l	0.005	0.003
Mn	0.001	b.d.l	b.d.l	0.001	b.d.l	b.d.l
Mg	b.d.l	b.d.l	b.d.l	b.d.l	b.d.l	b.d.l
Ca	b.d.l	b.d.l	b.d.l	1.192	0.191	0.187
Na	0.048	0.065	0.069	0.779	0.789	0.814
K	0.866	0.918	0.924	0.014	0.007	0.007
An (%)				19.467	19.379	18.556
Ab (%)	5.234	6.644	6.947	79.113	79.871	80.718
Or (%)	94.766	93.356	93.053	1.42	0.75	0.726

Table 2. Representative chemical analyses for the Catingueira pluton. Table of average of the obtained values.

Catingueira pluton					
		K-feldspar		Plagioclase	
Bulk Composition (XRF)		Porphyroclasts	Recrystallized	Porphyroclasts	Recrystallized
SiO ₂	60.08	63.887	63.613	61.514	63.948
TiO ₂	79.87	0.004	0.067	b.d.l	b.d.l
Al ₂ O ₃	101.96	19.922	19.703	24.803	22.019
FeO	71.84	0.032	0.01	0.269	0.25
MnO	70.94	0.022	0.026	0.058	0.04
MgO	40.30	b.d.l	0.004	0.014	0.044
CaO	56.08	b.d.l	b.d.l	4.122	3.225
Na ₂ O	61.98	0.737	0.864	9.292	9.738
K ₂ O	94.20	15.58	15.437	0.156	0.285
Cr ₂ O ₃	b.d.l	b.d.l	0.012	0.036	b.d.l
Total		100.18	99.73	100.67	99.63
Si		2.94	2.715	2.715	2.832
Ti		1.1	b.d.l	b.d.l	b.d.l
Al		b.d.l	1.29	1.29	1.149
Cr		b.d.l	0.002	0.002	b.d.l
Fe		0.001	0.001	0.001	0.009
Mn		0.001	b.d.l	b.d.l	0.002
Mg		b.d.l	b.d.l	b.d.l	0.003
Ca		b.d.l	1.192	1.192	0.153
Na		0.066	0.786	0.786	0.836
K		0.914	0.012	0.012	0.016
An (%)		0	19.377	19.377	15.222
Ab (%)		6.707	79.372	79.372	83.176
Or (%)		93.293	1.25	1.25	1.602

4.4.5. Zircon U-Pb geochronology

One sample was collected in NW portion of the Santa Terezinha pluton (PUR-02D - 7° 6'16.95"S, 37°25'56.58"E) for geochronological analysis via LA-ICP-MS.

This rock is zircon poor and most of them are strongly discordant, highly fractured or show strong evidence of metamictization. The small number of the recovered zircon crustals show Th/U ratios ranging from 0.38 to 0.63 (Table 3). They have a mean size of 120 µm, euhedral to subhedral shapes, and axial ratios around 1:3, commonly exhibiting bipyramidal crystallographic habit (Fig.10a). The internal structure revealed by backscatter electron (BSE) images presents oscillatory zoning, microfractures with radial to random patterns, and a spongy texture, probably due to inner metamictization (Fig.10a). Small inclusions of unidentified phases are present both in the core and rims of the zircon crystals.

Twenty-nine spots were performed on the sample PUR-02D, in which seven spots with concordance varying from 99.58 to 100.92% were plotted in the Concordia diagram (Table 3, Fig. 10a). Three of them were used to calculate a Concordia age of 625 ± 7 Ma (MSWD = 0.84), interpreted as the crystallization age of the pluton, whereas early Neoproterozoic ages are interpreted as inheritance from the host rocks (Fig. 10b).

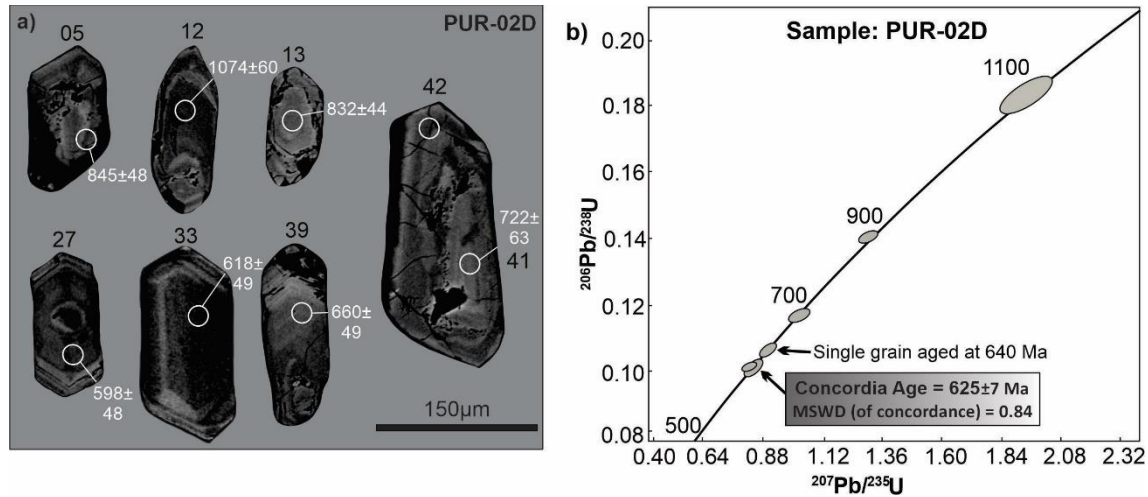


Figure 10. (a) Backscatter electron images of zircon grains from samples PUR-02D, Santa Terezinha pluton. (b) Concordia plot for the PUR-02C zircon spots with a lower 5% discordance displaying the main age of 625 ± 7 Ma.

Table 3 LA-MC-ICP-MS U-Pb data used for U-Pb age calculation for the Teresinha pluton.

Grain spot	Isotopic ratios						Ages								
	207Pb/206Pb	±(2σ)	207Pb/235U	±(2σ)	206Pb/238U	±(2σ)	207Pb/206Pb	±(2σ)	207Pb/235U	±(2σ)	206Pb/238U	±(2σ)	Rho	Th/U	Conc. (%)
PUR-02D-05	0.07	2.32	1.33	2.41	0.14	0.65	845	48	860	14	866	5	0.27	0.38	100.79
PUR-02D-12	0.07	3.13	1.91	3.89	0.18	2.31	1074	60	1082	25	1087	23	0.54	0.63	100.43
PUR-02D-13	0.07	2.14	2.29	2.35	0.14	0.1	832	44	844	13	850	8	0.42	0.43	100.74
PUR-02D-27	0.06	2.21	0.84	2.6	0.1	1.36	598	47	620	12	626	8	0.52	0.42	100.92
PUR-02D-33	0.06	2.25	0.85	3.05	0.1	2.05	617	49	624	14	625	12	0.67	0.46	100.18
PUR-02D-39	0.06	2.26	0.91	2.8	0.11	1.63	660	49	656	13	656	10	0.58	0.51	99.85
PUR-02D-41	0.06	2.95	1.03	3.25	0.12	1.38	722	63	719	17	716	9	0.42	0.42	99.58

4.5.Discussion

4.5.1. Deformation mechanisms in the mylonitic gneisses

Microstructures and EBSD analysis indicate that quartz grains are deformed by dislocation creep, mainly at low to medium greenschist-facies conditions (Hirth and Tullis, 1992). The recrystallized quartz grains occur as polycrystalline ribbons, with sizes around 30 μm , rounded to polygonal shapes, lobate boundaries, and undulose extinction. The PT172 and PT247 pole figures present small maxima of the [0001] axis at the periphery of the diagram, close to Z, which suggests recrystallization along the basal $\langle a \rangle$ slip system combined with the activation of rhomb planes (Vauchez, 1980; Schmid and Casey, 1986; Law, 1990). Furthermore, correlated misorientation angle distributions show high-frequencies of low-angle misorientations for all samples, with peaks at angles between 5 and 10° (Fig. 7a-e).

On the other hand, the patterns observed in PT249, PT250, and GPT2 show [0001] maxima located at the center of the pole figure, in Y, indicating that recrystallization occurred mainly through slip along prism planes (Schmid and Casey, 1986; Stipp *et al.* 2002a, 2004). These samples show uncorrelated distributions that deviate from the theoretical random curve, which is accompanied by high-frequency peaks of correlated distributions at angles of 40-60° (Fig. 7c).

Taken together, these observations suggest that the crystallographic preferred orientation of quartz grains in the mylonitic gneisses mainly results from rotational recrystallization along basal, rhomb and prism planes (Stipp *et al.*, 2002a. 2004; Stipp and Kunze, 2008). Basal $\langle a \rangle$, rhomb $\langle a+c \rangle$ and prism $\langle a \rangle$ slip systems have been reported as being typical of mylonitization at upper-greenschist to lower-amphibolite facies conditions (Fitz Gerald *et al.* 2006; Toy *et al.* 2008).

The K-feldspar and plagioclase porphyroclasts display intragranular microfractures that crosscut the clasts forming angular fragments ($\pm 800 \mu\text{m}$; Fig. 4f), with an offset of up to 50 μm (Fig. 4c, d, f). This observation suggests that the fragments within the fractures are the product of mechanical fragmentation of larger clasts. In addition, the presence of lobate boundaries, undulose extinction, and deformation twins in the clasts indicates that there is limited solid-state strain within the larger porphyroclasts (Faleiros *et al.* 2010).

Hence, the current dataset of microstructures and CPO analyses allows us to postulate that mylonitization in the south border of the Patos shear zone was attained mainly via

a combination of dynamic recrystallization of quartz aggregates and mechanical fragmentation of feldspar porphyroclasts. Such partitioning of recrystallization mechanisms is commonly observed in middle- to upper-greenschist facies shear zones deformed at mid-crustal levels (FitzGerald & Stunitz 1993, Stipp *et al.* 2002, Castellan *et al.* 2020).

4.5.2. Mylonitization in the Santa Terezinha and Catingueira plutons

Viegas *et al.* (2014) presented EBSD analysis for these granitoids and interpreted their recrystallization mechanisms as being accommodated mainly by dislocation creep at upper greenschist/lower amphibolite facies conditions (~500°C). These data are in agreement with the EBSD analysis for the host rocks of the plutons presented in this study, and corroborate with the microstructures observed in the plutons.

The granitic bodies show quartz polycrystalline ribbons with polygonal to irregular shapes, and straight boundaries defining triple junctions (Fig.5b, 6d). Undulose extinction, subgrain boundaries with ca. 50 µm and straight to curved boundaries are also observed. These microstructures suggest that quartz was recrystallized through transitional bulging recrystallization-subgrain rotation recrystallization (BLG-SGR) mechanisms (Stipp *et al.* 2002a; Passchier & Trouw, 2005; Faleiros *et al.* 2010).

The porphyroclasts of K-feldspar and plagioclase have sub-elliptical to rounded shapes and are mainly fractured, producing fragments of intermediate size ($\pm 100 \mu\text{m}$) between porphyroclasts and matrix (Fig.5e-f). Plagioclase and K-feldspar grains in the recrystallized matrix have similar chemical compositions to that of the porphyroclasts (Fig.8), represented mainly by oligoclase and K-sanidine, respectively (Fig. 9). These observations suggest that the smaller fragments were the product of mechanical fragmentation of larger clasts. On the other hand, the Catingueira pluton shows a difference between the plagioclase porphyroclasts and the fine-grained plagioclase of the recrystallized matrix (Fig.8d). This difference implies that grain size reduction in feldspars was the result of combined fracturing + nucleation/recrystallization, possibly enhanced by the presence of fluids (Fitz Gerald & Stünitz, 1993; Castellan *et al.* 2020).

Such observations indicate that the microstructure of the plutons is similar to the fabric of the mylonitic gneisses and point to the deformation/recrystallization at upper-greenschist/lower-amphibolite facies conditions (FitzGerald & Stunitz 1993, Stipp *et al.* 2002, Castellan *et al.* 2020). The microstructures observed in quartz and feldspar crystals, and the

CPO analyses of the plutons (Viegas *et al.*, 2014) suggest the activity of dislocation creep as the main deformation mechanism in the Santa Terezinha and Catingueira granitoids (Hirth & Tullis, 1992; Stipp *et al.* 2002a).

4.5.3. Chronology of granitoid magmatism in the southern border of the Patos shear zone

Magmatic events in the Patos shear zone have been constrained as being an integral part of the evolution of the structure. Evidence for pre-kinematic pluton emplacement was presented by Archanjo *et al.* (2008), who constrained the fabrics and the age of emplacement of the Teixeira batholith, which outcrops at the southern boundary of the Patos shear zone. The combined structural data of N-S trending, perpendicular magnetic fabrics and an U-Pb SHRIMP age of 591 ± 5 Ma presented by the authors were interpreted as a pre-kinematic emplacement setting for the Teixeira batholith, thus suggesting that transcurrent motion in the Patos shear zone is younger than ~ 590 Ma (Archanjo *et al.*, 2008).

Synkinematic partial melting events in the central portion of the shear zone have been presented by Viegas et al. (2014), who analyzed the recrystallized rims of zircon grains from diatexites emplaced in the central portion of the shear zone. The obtained U-Pb ages of ca. 565 Ma were interpreted by the authors as the peak conditions for the main metamorphic/deformational event in the Patos shear zone.

The Santa Terezinha granite shows an elongated shape that is concordant with the main ESE-WNW trend of the Patos Shear Zone (Fig.1). This concordant shape suggests that the emplacement of the pluton was synkinematic in relation to the shear zone. The mean result calculated in the Concordia diagram for this pluton provides an early Ediacaran age of 625 ± 7 Ma (Figs. 10a, 11a), which is considered the best estimate for magmatic crystallization of this granitoid.

The early Ediacaran age of 625 Ma acquired for the Santa Terezinha pluton offers an alternative interpretation for the timing of deformation and magmatism events in the southern border of the Patos shear zone, although we recognize that more geochronological data is needed. Since the pluton has an elongated shape, is mylonitized, and is concordant with the main trend of the structure, the age of 625 Ma suggests that magmatic crystallization of the time interval ranging from pluton emplacement to subsequent crystallization and solidification may have been protracted, lasting for at least ~ 45 Ma.

Such constraints may be able to reconcile the apparent contrasting observations of an early emplacement and a syntectonic deformation of the pluton. The combination of geochronological and structural data presented in this study suggest that the Santa Terezinha granite was emplaced before the main strike-slip shearing of the Patos shear zone, currently dated at ~ 565 Ma (Viegas *et al.*, 2014). The pluton remained in a molten state for ~ 40 Ma and recorded the solid-state deformation of the Patos shear zone during its cooling path. The slow to moderate cooling rates mainly in the central branch of the shear zone have been recently constrained by Archanjo *et al.* (2021), who constrained cooling rates of ~ 17° C/Ma in the central sector of the shear zone using the closure temperatures of hornblende and biotite during 40Ar/39Ar dating.

Repeated magmatic production events within the shear zone may have contributed to the maintenance of a high-temperature gradient that resulted in solid-state deformation in the Santa Terezinha granite during its cooling path. Such events, which lasted until late Neoproterozoic times, are associated with partial melting and significant rheological weakening of large domains of the northern Borborema Province and the southern Nigerian shield (Archanjo *et al.*, 2013), as evidenced by the continental connections of the Patos shear zone and the Seridó schist belt into the East Nigeria shear zone and the Igarra and the Illesha metasedimentary belts (Hurley *et al.* 1967; Brito Neves *et al.* 2002; Arthaud *et al.* 2008; Caby *et al.* 2008; Van Schmus *et al.* 2008; Ganade de Araújo *et al.* 2016).

4.6. Conclusions

Based on meso- and microscale structures, bulk rock and mineral chemistry, and U-Pb geochronology analysis, the following conclusions can be drawn from this study:

1. The microstructures and CPO analysis presented from the mylonitic gneisses indicate an interplay between brittle and ductile deformation mechanisms in south border of the Patos Shear Zone. Quartz is mainly recrystallized through solid state, subgrain rotation recrystallization, while the feldspar occurs fractured and heterogeneous, sometimes fluid assisted dissolution precipitation. Furthermore, the CPO of quartz reveal rotational recrystallization along basal $\langle a \rangle$, rhomb $\langle a+b \rangle$, and prism $\langle a \rangle$ planes, typical of mylonitization at upper greenschist to lower-amphibolite facies shear zones, deformed at mid-crustal levels.

2. The Santa Terezinha and Catingueira plutons presented recrystallization accommodated mainly by dislocation creep at upper greenschist/lower amphibolite facies conditions (~500°C), similar to the host mylonitic gneisses, and corroborating with Viegas *et al.* 2014. The microstructures reveal that quartz was recrystallized through transitional BLG-SGR regimes, while the feldspars show mechanical fragmentation, possibly fluid assisted dissolution precipitation.

3. The Santa Terezinha pluton presents an early Ediacaran age of 625 ± 7 Ma, which was considered as the best estimate for magmatic crystallization of the pluton.

4. The combination of geochronological and structural data presented in this study suggests that the Santa Terezinha granite was emplaced before the main strike-slip shearing of the Patos shear zone, currently dated at ~ 565 Ma (Viegas *et al.*, 2014). Repeated magmatic events within the shear zone may have contributed to the maintenance of the high-temperature gradient that enabled remaining the pluton in a molten state for ~ 40 Ma, recording the solid-state deformation of the Patos shear zone during its cooling path.

References

- Almeida F.F.M. 1967. Origem e evolução da plataforma brasileira. Boletim DNPM/DGM, 241. 36 p.
- Almeida F.F.M., Hasui Y., Brito Neves B.B., Fuck R.A. 1981. Brazilian structural provinces: an introduction. Earth Science Reviews, 17(1-2):1-29.
- Archajo, C. J., Bouchez, J.-L., Corsini, M., & Vauchez, A., 1994. The Pombal granite pluton: Magnetic fabric, emplacement and relationships with the Brasiliano strike-slip setting of NE Brazil (Paraiba State). Journal of Structural Geology, 16(3), 323–335. [http://doi:10.1016/0191-8141\(94\)90038-8](http://doi:10.1016/0191-8141(94)90038-8).
- Archajo C.J., Silva E.R., Caby R. 1999. Magnetic fabric and pluton emplacement in a transpressive shear zone system: the Itaporanga porphyritic granitic pluton (Northeast Brazil). Tectonophysics, 312(2-4):331-345. [https://doi.org/10.1016/S0040-1951\(99\)00176-6](https://doi.org/10.1016/S0040-1951(99)00176-6).
- Archajo, C.J., Trindade, R.I.F., Bouchez, J.L., Ernesto, M., 2002. Granite fabrics and regional-scale strain partitioning in the Seridó belt (Borborema Province, NEBrazil). Tectonics 21 (1), <http://dx.doi.org/10.1029/2000TC001269>.

Archanjo, C. J., & Fetter, A. H., 2004. Emplacement setting of the granite sheeted pluton of Esperança (Brasiliano orogen, Northeastern Brazil). *Precambrian Research*, 135(3), 193–215. <http://doi:10.1016/j.precamres.2004.08.008>.

Archanjo, C.J., Hollanda, M.H.B.M., Rodrigues, S.W.O., Brito Neves, B.B., Armstrong, R., 2008. Fabrics of pre- and syntectonic granite plutons and chronology of shearzones in the Eastern Borborema, NE Brazil. *Journal of Structural Geology* 30, 310–326.

Archanjo, C.J., Viegas, L.G., Hollanda, M.H.B.M., Souza, L.C., Liu, D., 2013. Timing of the HT/LP transpression in the Neoproterozoic Seridó Belt (Borborema Province, Brazil): constraints from U–Pb (SHRIMP) geochronology and implications for the connections between NE Brazil and West Africa. *Gondwana Research* 23, 701–714, <http://dx.doi.org/10.1016/j.gr.2012.05.005>.

Archanjo, C.J., Hollanda, M.H.B.M., Viegas, L.G.F. 2021. Late Ediacaran lateral-escape tectonics as recorded by the Patos shear zone (Borborema Province, NE Brazil). *Brazilian Journal of Geology*, 51(2): e20200132. <https://doi.org/10.1590/2317-4889202120200132>.

Brito Neves B.B., Santos E.J., Van Schmus W.R. 2000. Tectonic history of the Borborema province. In: Cordani U.G., Milani E.J., Thomaz Filho A., Campos D.A. (Eds.). *Tectonic Evolution of South América*. Rio de Janeiro, 31st International Geological Congress, p. 151-182.

Brito Neves B.B., Passarelli C.R., Basei M.A.S., Santos E.J. 2003. Idades U-Pb em zircão de alguns granitos clássicos da Província Borborema. *Geologia USP Série Científica*, 3:25-38. <https://doi.org/10.5327/S1519-874X2003000100003>.

Brown, M., Solar, G.S., 1998. Granite ascent and emplacement during contractional deformation in convergent orogens. *Journal of Structural Geology* 20 (9/10), 1365-1393.

Brown, M., & Solar, G. S., 1999. The mechanism of ascent and emplacement of granite magma during transpression: a syntectonic granite paradigm. *Tectonophysics*, 312(1), 1–33. [http://doi:10.1016/s0040-1951\(99\)00169-9](http://doi:10.1016/s0040-1951(99)00169-9)

Castellan, P., Viegas, G., Faleiros, F.M., 2020. Brittle-ductile fabrics and P-T conditions of deformation in the East Pernambuco shear zone (Borborema Province, NE Brazil). *J. Geol. Soc.* 178, jgs2020-109. <https://doi.org/10.1144/jgs2020-109>.

Caxito, F.A., Santos, L.C.M.L., Ganade, C.E., Bendaoud, A., Fettous, E., Bouyo, M.H. 2020. Toward an integrated model of geological Evolution for NE Brazil-NW Africa: the Borborema Province and its connections to the Trans-Saharan (Benino-Nigerian and Tuareg shields) and Central African orogens. *Brazilian Journal of Geology* 50, e20190122. <https://doi.org/10.1590/2317-4889202020190122>.

Corsini, M., Vauchez, A., Archanjo, C.J., Jardim de Sá, E.F., 1991. Strain transfer at a continental scale from a transcurrent shear zone to a transpressional fold belt: the Patos-Seridó belt system, north-eastern Brazil. *Geology* 19, 586–589.

Faleiros, F.M., Campanha, G.A.C., Maria, R. & Fuzikawa, K. 2010. Quartz recrystallizations regimes, c-axis texture transition and fluid inclusion reequilibration in a prograde greenschist to amphibolite facies mylonite zone (Ribeira Shear Zone, SE Brazil). *Tectonophysics*, 485, 193-214, <https://doi.org/10.1016/j.tecto.2009.12.014>

- Fitz Gerald, J.D. & Stünitz, H. 1993. Deformation of granitoids at low metamorphic grade. I: Reactions and grain size reduction. *Tectonophysics*, 221, 269-297, [https://doi.org/10.1016/0040-1951\(93\)90163-E](https://doi.org/10.1016/0040-1951(93)90163-E)
- Fitz Gerald, J. D., Mancktelow, N. S., Pennacchioni, G., & Kunze, K., 2006. Ultrafine-grained quartz mylonites from high-grade shear zones: Evidence for strong dry middle to lower crust. *Geology*, 34(5), 369. <http://doi:10.1130/g22099>.
- Guimarães, I.P., Silva Filho, A.F., Silva Filho, Almeida, C.N., Van Schmus, W.R., Araújo, J.M.M., Melo, S.C. & Melo, E.B. 2004. Brasiliano (Pan-African) granitic magmatism in the Pajeú-Paraíba belt, Northeast Brazil: an isotopic and geochronological approach. *Precambrian Research*, 135, 23-53, <https://doi.org/10.1016/j.precamres.2004.07.004>
- Hirth, G. & Tullis, J. 1992. Dislocation creep regimes in quartz aggregates. *Journal of Structural Geology*, 14, 145-159, [https://doi.org/10.1016/0191-8141\(92\)90053-Y](https://doi.org/10.1016/0191-8141(92)90053-Y)
- Hollanda, M.H.B.M., Archanjo, C.J., Souza, L.C., Armstrong, R., Vasconcelos, P.M., 2010. Cambrian mafic to felsic magmatism and its connections with transcurrent shear zones of the Borborema Province (NE Brazil): implications for the late assembly of the West Gondwana. *Precambrian Research* 178, 1–14. <http://dx.doi.org/10.1016/j.precamres.2009.12.004>.
- Horstwood, M. S. A., Košler, J., Gehrels, G., Jackson, S. E., McLean, N. M., Paton, C., Schoene, B., 2016. Community-Derived Standards for LA-ICP-MS U-(Th-)Pb Geochronology - Uncertainty Propagation, Age Interpretation and Data Reporting. *Geostandards and Geoanalytical Research*, 40(3), 311–332. <http://doi:10.1111/j.1751-908x.2016.00379>.
- Hutton, D.H.W., 1988. Granite emplacement mechanisms and the tectonic controls: inferences from deformation studies. *Transactions of the Royal Society of Edinburgh: Earth Sciences* 79, 245e255.
- Jackson, S.E., Pearson, N.J., Griffin, W.L., Belousova, E.A., 2004. The application of laser ablation-inductively coupled plasma-mass spectrometry to in situ U-Pb zircon geochronology. *Chemical Geology* 211, 47–69.
- Law, R. D. (1990) Crystallographic fabrics: a selective review of their applications to research in structural geology. In *Deformation Mechanisms, rheology and tectonics*, eds R. Knipe and E. Rutter, pp. 335-352. Geological Society of London. Special Publication 54.
- LUDWIG, K. R., 1993. New Isoplot Version 2.2. Berkeley Geochronology Center, February.
- Neves, S.P., Vauchez, A., Archanjo, C.J., 1996. Shear-zone controlled magma emplacement or magma-assisted nucleation of shear zones? Insights from northeastBrazil. *Tectonophysics* 262, 349–365.
- Neves, S.P., Vauchez, A., Féraud, G., 2000. Tectono-thermal evolution, magma emplacement, and shear zone development in the Caruaru area (Borborema Province, NE Brazil). *Precambrian Research* 99, 1–32.
- Neves., S.P. 2003. Proterozoic history of the Borborema Province (NE Brazil): correlations with neighboring cratons and Pan-African belts and implications for the evolution of western Gondwana. *Tectonics*, 22, 1030, <https://doi.org/10.1029/2001TC001352>

- Neves, S.P., Bruguier, O., Vauchez, A., Bosch, D., Silva, J.M.R., Mariano, G., 2006. Timing of crustal formation, deposition of supracrustal sequences and Transamazonian and Brasiliano metamorphism in eastern Borborema Province (NE Brazil): Implications for western Gondwana assembly. *Precambrian Research*. 149, 197-216.
- Passchier, C.W. & Trouw, R.A.J. 2005. *Microtectonics*. 2nd edn. Springer, Berlin.
- Paterson, S.R., Fowler Jr., T.K., Schmidt, K.L., Yoshinobu, A.S., Yuan, E.S., Miller, R.B., 1998. Interpreting magmatic fabric patterns in plutons. *Lithos* 44, 53e82.
- Paterson, S. R. & Tobisch, O. T. 1992. Rates of geological processes in magmatic arcs: implications for the timing and nature of pluton emplacement and wall-rock deformation. *J. Struct. Geol.* 14, 291-300
- Paton, C., Hellstrom, J., Paul, B., Woodhead, J. and Hergt, J. (2011) Iolite: Freeware for the visualisation and processing of mass spectrometric data. *Journal of Analytical Atomic Spectrometry*. doi:10.1039/c1ja10172b.
- Petrus, J.A. and Kamber, B.S. (2012) VizualAge: A novel approach to laser ablation ICP-MS U-Pb geochronology data reduction. *Geostandards and Geoanalytical Research* 36(3), p. 247-270.
- Rosenberg, C.L., 2004. Shear zones and magma ascent: a model based on a review of the Tertiary magmatism in the Alps. *Tectonics*, 23, TC3002. <http://doi:10.1029/2003TC001529>.
- Santos, E.J., Medeiros, V.C., 1999. Constraints from granitic plutonism on Proterozoic crustal growth of the Transverse Zone, Borborema Province, NE Brazil. *Revista Brasileira de Geociências* 29, 73–84.
- Schmid, S.M., Casey, M., 1986. Complete fabric analysis of some commonly observed quartz [c]-axis patterns. In: Hobbs, B.E., Heard, H.C. (Eds.), *Mineral and Rock Deformation: Laboratory Studies*, vol. 36. American Geophysical Union, *Geo-physical Monograph*, pp. 263–286.
- Schmidt, K. L., & Paterson, S. R., 2000. Analyses fail to find coupling between deformation and magmatism. *Eos, Transactions American Geophysical Union*, 81(18), 197. <http://doi:10.1029/00eo00133>.
- Sial A.N. 1986. Granite-types in northeast Brazil: current knowledge. *Revista Brasileira de Geociências*, 16(1):54-72.
- Stipp, M., Stünitz, H., Heilbronner, R. & Schmid, S.M. 2002a. The eastern Tonale fault zone: a ‘natural laboratory’ for crystal plastic deformation of quartz over a temperature range from 250 to 700°C. *Journal of Structural Geology*, 24, 1861-1884, [https://doi.org/10.1016/S0191-8141\(02\)00035-4](https://doi.org/10.1016/S0191-8141(02)00035-4)
- Stipp, M., Fügenschuh, B., Gromet, L.P., Stünitz, H., Schmid, S.M., 2004. Contemporaneous plutonism and strike-slip faulting: a case study from the Tonale fault zone north of the Adamello pluton (Italian Alps). *Tectonics* 23, TC3004. <http://doi:10.1029/2003TC001515>.

- Stipp, M., & Kunze, K., 2008. Dynamic recrystallization near the brittle-plastic transition in naturally and experimentally deformed quartz aggregates. *Tectonophysics*, 448(1-4), 77–97. <http://doi:10.1016/j.tecto.2007.11.041>
- Toy, V. G., Prior, D. J., & Norris, R. J., 2008. Quartz fabrics in the Alpine Fault mylonites: Influence of pre-existing preferred orientations on fabric development during progressive uplift. *Journal of Structural Geology*, 30(5), 602–621. <http://doi:10.1016/j.jsg.2008.01.001>.
- Van Schmus W.R., Brito Neves B.B., Hackspacher P., Babinski M. 1995. U/Pb and Sm/Nd geochronologic studies of eastern Borborema Province, northeastern Brazil: initial conclusions. *Journal of South American Earth Sciences*, 8(3-4):267-288. [https://doi.org/10.1016/0895-9811\(95\)00013-6](https://doi.org/10.1016/0895-9811(95)00013-6).
- Van Schmus, W.R., Oliveira, E.P., Silva Filho, A.F., Toteu, S.F., Penaye, J., Guimaraes,I.P., 2008. Proterozoic links between the Borborema Province, NE Brazil, and the Central African Fold Belt. In: Pankhurst, R.J., Trouw, R.A.J., Brito Neves, B.B., DeWit, M.J. (Eds.), West Gondwana: Pre-Cenozoic Correlations Across the South Atlantic Region, vol. 294. Geological Society of London, Special Publications, pp.69–99, <http://dx.doi.org/10.1144/SP294.5>.
- Van Schmus W.R., Kozuch M., Brito Neves B.B. 2011. Precambrian history of the Zona Transversal of the Borborema Province, NE Brazil: Insights from Sm-Nd and U-Pb geochronology. *Journal of South American Earth Sciences*, 31(2-3):227-252. <https://doi.org/10.1016/j.jsames.2011.02.010>.
- Vauchez, A. 1980. Ribbon texture and deformation mechanisms of quartz in a mylonitized granite of Great Kabylia (Algeria). *Tectonophysics*, 67, 1-12, [https://doi.org/10.1016/0040-1951\(80\)90160-2](https://doi.org/10.1016/0040-1951(80)90160-2).
- Vauchez A., Neves S., Caby R., Corsini M., Egydio-Silva M., Arthaud M., Amaro V. 1995. The Borborema shear zone system, NE Brazil. *Journal of South American Earth Sciences*, 8(3-4):247-266. [https://doi.org/10.1016/0895-9811\(95\)00012-5](https://doi.org/10.1016/0895-9811(95)00012-5).
- Vauchez, A., Neves, S.P., 1997. Transcurrent shear zones and magma emplacement in Neoproterozoic belts of Brazil. In: Bouchez, J.L., et al. (Eds.), *Granite: From Segregation of Melt to Emplacement Fabrics*. Kluwer, Boston, pp. 275e293.
- Viegas L.G.F., Archanjo C.J., Hollanda M.H.B.M., Vauchez A. 2014. Microfabrics and zircon U-Pb (SHRIMP) chronology of mylonites from the Patos shear zone (Borborema Province, NE Brazil). *Precambrian Research*, 243:1-17. <https://doi.org/10.1016/j.precamres.2013.12.020>.
- Viegas, L.G., Menegon, L., Archanjo, C.J. 2016. Brittle grain-size reduction of feldspar, phase mixing and strain localization in granitoids at mid-crustal conditions (Pernambuco shear zone, NE Brazil). *Solid Earth* 7, 375-396.
- Vigneresse, J.L., 1995. Control of granite emplacement by regional deformation. *Tectonophysics* 249, 173e186.
- Whitney, D. L., Evans B. W., 2010. Abbreviations for names of rock-forming minerals. *American Mineralogist*, 95, 185-187. <http://doi:10.2138/am.2010.3371>.
- Wiedenbeck, M., Allé, P., Corfu, F., Griffin, W. L., Meier, M., Oberli, F., Spiegel, W., 1995. Three Natural Zircon Standards for U-Th-Pb, Lu-Hf, Trace Element and REE Analyses.

Geostandards and Geoanalytical Research, 19(1), 1–23. <http://doi:10.1111/j.1751-908x.1995.tb00147>.

Weinberg, R.F., Sial, A.N. & Mariano, G. 2004. Close spatial relationship between plutons and shear zones. Geology, 32, 377-380, <https://doi.org/10.1130/0091-7613-33.1.e72>

5. CONSIDERAÇÕES FINAIS

Este estudo teve como objetivo caracterizar estrutural e espacialmente, bem como cronologicamente, os plútôns graníticos e suas rochas encaixantes com relação à deformação de baixa a média temperatura ocorrente na porção sul da ZCP. Para isto, foi realizado estudo de campo em um setor da porção sul do lineamento (entre a cidade de Patos e Coremas), caracterização estrutural das estruturas deformacionais existentes nos plútôns e nas rochas encaixantes, análises de orientação preferencial cristalográfica e química mineral de feldspatos (clastos e matriz) dos plútôns, além de análise U-Pb em zircão no plúton Santa Terezinha.

As principais conclusões são apresentadas nos seguintes tópicos:

5.1.Caracterização estrutural

A integração entre as etapas de campo e análise microestrutural quantitativa permitiu observar o padrão de metamorfismo principalmente sob fácies xisto verde na porção sul da ZCP. Este setor da zona de cisalhamento apresenta gnaisses graníticos, rochas metavulcânicas e metassedimentares, ambas intrudidas por plútôns graníticos. As rochas comumente apresentam foliação milonítica E-W, marcada sobretudo por *ribbons* de quartzo alongados, lamelas de biotita alongadas e porfiroclastos de K-feldspato e plagioclásio estirados. A foliação milonítica foi observada em maior evidência nos granitos gnáissicos e nas rochas metassedimentares, ocorrendo localmente transição para bandas ultramiloníticas. Esta transição é caracterizada pela diminuição da distribuição e porcentagem de matriz, diminuição progressiva no tamanho e da presença de porfiroclastos, maior ocorrência de lamelas de biotita e muscovita marcando a foliação, bem como estiramento dos clastos de feldspato. Por outro lado, os plútôns graníticos exibem variedades protomiloníticas, miloníticas e localmente ultramiloníticas, estas últimas observadas como bandas centimétricas no plúton Catingueira. Os plútôns apresentam formas alongadas e tabulares, conforme a foliação milonítica principal E-W/WNW-ESSE observada na ZCP.

As microestruturas e as análises EBSD para os cristais de quartzo dos gnaisses miloníticos indicam uma interação entre mecanismos de deformação rúptil e dúctil na porção sul da ZCP. Os cristais de quartzo apresentam recristalização principalmente por meio de recristalização no estado sólido e rotação de subgrãos, enquanto que os feldspatos ocorrem fraturados e heterogêneos, com deformação no estado sólido localizada nos porfiroclastos maiores. Ainda, a orientação preferencial cristalográfica dos cristais de quartzo revela recristalização rotacional ao longo dos planos basal $\langle a \rangle$, romboédrico $\langle a+c \rangle$ e prismático $\langle a \rangle$.

Estas características indicam milonitização em fácies xisto verde alto a anfibolito inferior nas zonas de cisalhamento, tendo a deformação ocorrido ao longo de níveis intermediários da crosta.

Os plútuns Santa Terezinha e Catingueira apresentam recristalização acomodada principalmente por fluência de deslocações (*dislocation creep*) sob condições de fácie xisto verde superior a anfibolito superior, condição similar à encontrada nas rochas encaixantes. As microestruturas observadas indicam que os cristais de quartzo recristalizados acomodaram a deformação pela transição dos regimes de migração lenta de borda de grãos (*bulging recrystallization – BLG*) e rotação de subgrãos (*subgrain rotation – SGR*). Os feldspatos, por outro lado, apresentam fragmentação mecânica que resulta na formação de misturas poliminerálicas finas, estas possivelmente derivadas de mecanismos de dissolução-precipitação assistidos por fluidos.

Estas evidências indicam que a porção sul da ZCP teve seu processo deformacional em condições típicas de transição rúptil-dúctil, em profundidades equivalentes a níveis crustais intermediários (~10-15 km).

5.2. Análise temporal do magmatismo granítico na borda sul da Zona de Cisalhamento Patos e suas implicações

A ZCP é caracterizada por diversos eventos magmáticos ao longo da sua evolução deformacional. Archanjo *et al.* (2008) apresentou para o batólito Teixeira, localizado a sul da ZCP, idade de cristalização de 591 ± 5 Ma, interpretada como de cristalização. O corpo granítico ainda apresenta, segundo os autores, trama magnética N-S, perpendicular ao padrão estrutural da ZCP (E-W). Interpretado como pré-cinemático com relação à movimentação transcorrente da ZCP, o batólito ocorre alongado conforme o padrão estrutural regional (E-W) e, por isso, os autores sugerem que o evento de transcorrência possa ter ocorrido próximo a 590 Ma.

Em 2014, Viegas e colaboradores apresentaram para a porção central da Zona de Cisalhamento Patos a idade de aproximadamente 565 Ma, essa interpretada como a melhor estimativa para as condições de pico metamórfico/deformacional na zona de cisalhamento.

Neste trabalho, dados U-Pb em zircão foram apresentados para o plúton Santa Terezinha, os quais apresentaram uma idade de 625 ± 7 Ma, interpretada como a idade de cristalização do granitoide. Devido ao formato alongado e concordante a ligeiramente oblíquo

com relação à foliação milonítica da ZCP, sugere-se que o alojamento e posterior solidificação deste plúton foram controlados pela zona de cisalhamento. A idade de 625 ± 7 Ma adquirida oferece uma interpretação alternativa para o tempo dos eventos de deformação e magmatismo ocorridos na borda sul do lineamento, apesar de reconhecermos que uma maior quantidade de dados geocronológicos é necessária.

Uma possível explicação para a idade de ca. 625 Ma para o plúton seria que a ascensão/colocação seguida da sua cristalização magmática e solidificação durou um intervalo de tempo de, pelo menos, 45 Ma, tendo em vista a proposta de Archanjo *et al.* (2008) de que o evento de transcorrência é mais jovem do que 590 Ma. Com isso, o plúton teria sido gerado em níveis crustais intermediários, possibilitando um resfriamento lento (~40 Ma) e uma cristalização sincrônica ao evento deformacional na zona de cisalhamento. Com relação à idade apresentada por Viegas *et al.* (2014) de ca. 565 Ma para o principal evento metamórfico ocorrido na ZCP, o plúton Santa Terezinha foi gerado anteriormente a este episódio e, permanecendo em estado fundido por cerca de 40 Ma, registrou a deformação em estado sólido da ZCP durante seu período de resfriamento. Taxas de resfriamento lentas a moderadas foram apresentadas por Archanjo *et al.* (2021) para migmatitos da porção central da ZCP por meio do método $^{40}\text{Ar}/^{39}\text{Ar}$, corroborando com o tempo de resfriamento proposto para o plúton Santa Terezinha neste trabalho.

A produção de repetidos eventos magmáticos durante o período de resfriamento do plúton Santa Terezinha podem ter mantido o gradiente de alta temperatura, possibilitando a deformação em estado sólido durante seu período de resfriamento. Estes eventos podem ser associados com eventos de fusão parcial e magmatismo ocorridos durante o Neoproterozoico tanto no norte da Borborema quanto nos terrenos do sul da Nigéria.

6. REFERÊNCIAS

- Almeida F.F.M. 1967. Origem e evolução da plataforma brasileira. Boletim DNPM/DGM, 241. 36 p.
- Almeida F.F.M., Hasui Y., Brito Neves B.B., Fuck R.A. 1981. Brazilian structural provinces: an introduction. Earth Science Reviews, 17(1-2):1-29.
- Archanjo, C.J., Hollanda, M.H.B.M., Rodrigues, S.W.O., Brito Neves, B.B., Armstrong, R., 2008. Fabrics of pre- and syntectonic granite plutons and chronology of shearzones in the Eastern Borborema, NE Brazil. Journal of Structural Geology 30,310–326.

- Archanjo, C.J., Hollanda, M.H.B.M., Viegas, L.G.F. 2021. Late Ediacaran lateral-escape tectonics as recorded by the Patos shear zone (Borborema Province, NE Brazil). *Brazilian Journal of Geology*, 51(2): e20200132. <https://doi.org/10.1590/2317-4889202120200132>.
- Brown, M., & Solar, G. S., 1999. The mechanism of ascent and emplacement of granite magma during transpression: a syntectonic granite paradigm. *Tectonophysics*, 312(1), 1–33. [http://doi:10.1016/s0040-1951\(99\)00169-9](http://doi:10.1016/s0040-1951(99)00169-9)
- Brito Neves B.B., Santos E.J., Van Schmus W.R. 2000. Tectonic history of the Borborema province. In: Cordani U.G., Milani E.J., Thomaz Filho A., Campos D.A. (Eds.). *Tectonic Evolution of South América*. Rio de Janeiro, 31st International Geological Congress, p. 151-182.
- Brito Neves B.B., Passarelli C.R., Basei M.A.S., Santos E.J. 2003. Idades U-Pb em zircão de alguns granitos clássicos da Província Borborema. *Geologia USP Série Científica*, 3:25-38. <https://doi.org/10.5327/S1519-874X2003000100003>.
- Neves, B. B. de B., Fuck, R. A., & Pimentel, M. M. 2014. The Brasiliano collage in South America: a review. *Brazilian Journal of Geology*, 44(3), 493–518. <http://doi:10.5327/z2317-4889201400030010>.
- Bühn, B., Pimentel, M. M., Matteini, M., & Dantas, E. L. (2009). High spatial resolution analysis of Pb and U isotopes for geochronology by laser ablation multi-collector inductively coupled plasma mass spectrometry (LA-MC-ICP-MS). *Anais Da Academia Brasileira de Ciências*, 81(1), 99–114. doi:10.1590/s0001-37652009000100011
- Corsini, M., Vauchez, A., Archanjo, C.J., Jardim de Sá, E.F., 1991. Strain transfer at a continental scale from a transcurrent shear zone to a transpressional fold belt: the Patos-Seridó belt system, north-eastern Brazil. *Geology* 19, 586–589.
- Corsini, M., Vauchez, A., & Caby, R. (1996). Ductile duplexing at a bend of a continental-scale strike-slip shear zone: example from NE Brazil. *Journal of Structural Geology*, 18(4), 385–394. doi:10.1016/0191-8141(95)00102-j
- Corsini, M., de Figueiredo, L. L., Caby, R., Féraud, G., Ruffet, G., & Vauchez, A., 1998. Thermal history of the Pan-African/Brasiliano Borborema Province of northeast Brazil deduced from $^{40}\text{Ar}/^{39}\text{Ar}$ analysis. *Tectonophysics*, 285(1-2), 103–117. doi:10.1016/s0040-1951(97)00192-3
- Dickin, A.P., Radiogenic Isotopic Geology. Cambridge, Gb: Cambridge University Press, 1997. p. 490
- Guimarães, I.P, Silva Filho, A.F., Silva Filho, Almeida, C.N., Van Schmus, W.R., Araújo, J.M.M., Melo, S.C. & Melo, E.B. 2004. Brasiliano (Pan-African) granitic magmatism in the Pajeú-Paraíba belt, Northeast Brazil: an isotopic and geochronological approach. *Precambrian Research*, 135, 23-53, <https://doi.org/10.1016/j.precamres.2004.07.004>
- Goldstein, J.I., Newburry, D.E., Joy, D.C., Lyman, C.E., Echlin, P., Lifshin, E., Sawyer, L., Michael, J.R. 2003. Scanning Electron Microscopy and X-Ray Microanalysis. New York, Kluwer Academic/Plenum Publisher, 689 p.

Hollanda, M.H.B.M., Archanjo, C.J., Souza, L.C., Armstrong, R., Vasconcelos, P.M., 2010. Cambrian mafic to felsic magmatism and its connections with transcurrent shear zones of the Borborema Province (NE Brazil): implications for the late assembly of the West Gondwana. *Precambrian Research* 178, 1–14. <http://dx.doi.org/10.1016/j.precamres.2009.12.004>.

Hutton, D.H.W., 1988. Granite emplacement mechanisms and the tectonic controls: inferences from deformation studies. *Transactions of the Royal Society of Edinburgh: Earth Sciences* 79, 245e255.

Kozuch, M., 2003. Isotopic and trace element geochemistry of Early Neoproterozoic gneissic and metavolcanic rocks in the Cariris Velhos Orogen of the Borborema Province, Brazil, and their bearing tectonic setting (Tese de Doutorado). Kansas University, Lawrence, p. 199.

Morales, L.F.G., Hinrichs, R., Fernandes, L.A.D. 2007. A técnica de Difração de Elétrons Retro-Espalhados (EBSD) em Microscópio Eletrônico de Varredura (MEV) e sua aplicação no estudo de rochas deformadas. *Revista Pesquisas em Geociências* 34, 19-34.

Neves, S.P., Vauchez, A., Féraud, G., 2000. Tectono-thermal evolution, magma emplacement, and shear zone development in the Caruaru area (Borborema Province, NE Brazil). *Precambrian Research* 99, 1–32.

Neves, B. B. de B., Fuck, R. A., & Pimentel, M. M. (2014). The Brasiliano collage in South America: a review. *Brazilian Journal of Geology*, 44(3), 493–518. doi:10.5327/z2317-4889201400030010

Prior, D.J., Boyle, A.P., Brenker, F., Cheadle, M.C., Day, A., Lopez, G., Peruzzo, L., Potts, G.J., Reddy, S., Spiess, R., Timms, N.E., Trimby, P., Wheeler, J., Zetterstrom, L. 1999. The application of electron backscatter diffraction and orientation contrast imaging in the SEM to textural problems in rocks. *American Mineralogist* 84, 1741-1759.

Randle, V. e Caul, M. 1996. Representation of electron backscatter diffraction data. *Materials Science and Technology* 12, 844-850. <https://doi.org/10.1179/mst.1996.12.10.844>

Santos, E.J., Medeiros, V.C., 1999. Constraints from granitic plutonism on Proterozoic crustal growth of the Transverse Zone, Borborema Province, NE Brazil. *Revista Brasileira de Geociências* 29, 73–84.

Santos, Lauro Montefalco de Lira. Processos Acrescionários na Porção Central de Gondwana: exemplos de Terrenos Alto Moxotó e Alto Pajeú da Província Borborema, NE do Brasil. 2017. 134f. Tese de Doutorado – Universidade de Brasília, Brasília, 2017.

Sial A.N. 1986. Granite-types in northeast Brazil: current knowledge. *Revista Brasileira de Geociências*, 16(1):54-72.

Van Schmus, W.R., Oliveira, E.P., Silva Filho, A.F., Toteu, S.F., Penaye, J., Guimarães, I.P., 2008. Proterozoic links between the Borborema Province, NE Brazil, and the Central African Fold Belt. In: Pankhurst, R.J., Trouw, R.A.J., Brito Neves, B.B., De Wit, M.J. (Eds.), *West Gondwana: Pre-Cenozoic Correlations Across the South Atlantic Region*, vol. 294. Geological Society of London, Special Publications, pp.69–99, <http://dx.doi.org/10.1144/SP294.5>.

Van Schmus W.R., Kozuch M., Brito Neves B.B. 2011. Precambrian history of the Zona Transversal of the Borborema Province, NE Brazil: Insights from Sm-Nd and U-Pb geochronology. *Journal of South American Earth Sciences*, 31(2-3):227-252. <https://doi.org/10.1016/j.jsames.2011.02.010>.

Vauchez A., Neves S., Caby R., Corsini M., Egydio-Silva M., Arthaud M., Amaro V. 1995. The Borborema shear zone system, NE Brazil. *Journal of South American Earth Sciences*, 8(3-4):247-266. [https://doi.org/10.1016/0895-9811\(95\)00012-5](https://doi.org/10.1016/0895-9811(95)00012-5).

Vauchez, A., Neves, S.P., 1997. Transcurrent shear zones and magma emplacement in Neoproterozoic belts of Brazil. In: Bouchez, J.L., et al. (Eds.), *Granite: From Segregation of Melt to Emplacement Fabrics*. Kluwer, Boston, pp. 275e293.

Viegas L.G.F., Archanjo C.J., Hollanda M.H.B.M., Vauchez A. 2014. Microfabrics and zircon U-Pb (SHRIMP) chronology of mylonites from the Patos shear zone (Borborema Province, NE Brazil). *Precambrian Research*, 243:1-17. <https://doi.org/10.1016/j.precamres.2013.12.020>.

Vigneresse, J.L., 1995. Control of granite emplacement by regional deformation. *Tectonophysics* 249, 173e186.

Weinberg, R.F., Sial, A.N. & Mariano, G. 2004. Close spatial relationship between plutons and shear zones. *Geology*, 32, 377-380, <https://doi.org/10.1130/0091-7613-33.1.e72>

Wenk, H.R. e Christie, J.M. 1991. Comments on the interpretation of deformation textures in rocks. *Journal of Structural Geology* 13, 1091-1110. [https://doi.org/10.1016/0191-8141\(91\)90071-P](https://doi.org/10.1016/0191-8141(91)90071-P).

7. ANEXOS

ANEXO I – Análises geoquímicas do plúton Santa Terezinha – clasto e matriz de K-feldspato e plagioclásio

Santa Terezinha pluton - Clast K-feldspar												
	1	2	3	4	5	6	7	8	9	10	11	12
SiO₂	64.749	64.534	64.982	64.529	64.01	65.237	63.161	65.207	62.788	65.82	63.828	65.669
TiO₂	0.018	0	0.004	0	0.013	0	0	0	0	0.067	0.04	0.027
Al₂O₃	19.661	19.473	19.621	19.703	19.703	18.260	18.270	18.772	18.315	18.524	18.205	18.568
FeO	0.002	0.038	0.034	0.047	0.002	0.016	0	0.358	0.004	0.073	0	0.002
MnO	0.012	0	0.029	0.01	0.027	0	0.003	0	0.004	0.003	0.031	0.008
MgO	0	0	0	0.017	0	0	0	0.011	0.015	0	0.007	0.001
Na₂O	0.645	0.529	0.532	0.625	0.658	0.463	0.781	1.121	0.382	0.54	0.863	2.073
CaO	0	0	0	0	0	0	0	0	0	0	0	0
K₂O	14.476	14.579	14.64	14.311	14.899	15.028	14.625	13.925	14.887	14.745	14.473	13.204
Cr₂O₃	0	0	0	0	0.038	0	0	0.017	0.018	0.023	0.033	0.008
NiO	0	0	0	0	0	0	0	0	0	0	0	0
Total	99.563	99.153	99.842	99.242	99.35	99.00432	96.83968	99.411	96.41344	99.79548	97.4802	99.56016
Si	3.007	3.012	3.012	3.007	2.975	3.053	3.012	3.03	3.014	3.057	3.025	3.028
Ti	0.001	0	0	0	0	0	0	0	0	0.002	0.001	0.001
Al	1.076	1.071	1.072	1.082	1.079	1.007	1.027	1.028	1.036	1.014	1.017	1.009
Cr	0	0	0	0	0.001	0	0	0.001	0.001	0.001	0.001	0
Fe	0	0.001	0.001	0.002	0	0.001	0	0.014	0	0.003	0	0
Mn	0	0	0.001	0	0.001	0	0	0	0	0	0.001	0
Mg	0	0	0	0.001	0	0	0	0.001	0.001	0	0	0
Ca	0	0	0	0	0	0	0	0	0	0	0	0
Na	0.058	0.048	0.048	0.056	0.059	0.042	0.072	0.101	0.036	0.049	0.079	0.185
K	0.858	0.868	0.866	0.851	0.883	0.897	0.89	0.825	0.912	0.874	0.875	0.777
An (%)	0	0	0	0	0	0	0	0	0	0	0	0
Ab (%)	6.642	5.226	5.234	6.224	6.29	4.473	7.507	10.901	3.753	5.272	8.309	19.264

Or (%)	93.658	94.774	94.766	93.776	93.71	95.527	92.493	89.099	96.247	94.728	91.691	80.736
---------------	--------	--------	--------	--------	-------	--------	--------	--------	--------	--------	--------	--------

Santa Terezinha pluton - matrix K-feldspar							
	core	rim	core	rim	core	rim	core
SiO₂	64.018	63.003	62.252	62.523	62.756	63.266	63.827
TiO₂	0	0	0	0	0.013	0	0
Al₂O₃	19.811	19.595	19.721	19.818	19.697	20.094	20.255
FeO	0.061	0.136	0.067	0.114	0.089	0.045	0.081
MnO	0.016	0.008	0.03	0	0.012	0.036	0
MgO	0	0.01	0.014	0.006	0	0	0.001
Na₂O	0	0	0	0	0	0.006	0
CaO	0.678	0.755	0.646	0.764	0.722	0.546	0.67
K₂O	15.555	15.412	15.588	15.553	15.418	15.571	15.374
Cr₂O₃	0.039	0.007	0.015	0.015	0.039	0.007	0
NiO	0	0	0	0	0	0	0
Total	100.178	98.926	98.333	98.793	98.746	99.571	100.209
Si	2.947	2.934	2.916	2.913	2.928	2.93	2.937
Ti	0	0	0	0	0	0	0
Al	1.075	1.075	1.089	1.088	1.083	1.097	1.098
Cr	0.001	0	0.001	0.001	0.001	0	0
Fe	0	0	0	0	0	0	0.003
Mn	0.001	0	0.001	0	0	0.001	0
Mg	0	0.001	0.001	0	0	0	0
Ca	0	0	0	0	0	0	0
Na	0.061	0.068	0.059	0.069	0.065	0.049	0.06
K	0.913	0.916	0.931	0.924	0.918	0.92	0.902
An (%)	0	0	0	0	0	0.031	0
Ab (%)	6.213	6.929	5.925	6.947	6.644	5.058	6.212
Or (%)	93.787	93.071	94.075	93.053	93.356	94.911	93.788

Santa Terezinha pluton - matrix plagioclase						
	rim	core	rim	core	rim	core
SiO₂	64.198	60.673	62.392	63.721	63.504	63.267
TiO₂	0.097	0	0	0	0.044	0
Al₂O₃	21.737	24.875	22.497	22.515	22.253	22.423
FeO	0.44	0.097	0.008	0.037	0.075	0.128
MnO	0.014	0.014	0	0	0	0
MgO	0.025	0	0	0	0.012	0
Na₂O	3.085	4.456	3.989	3.879	3.878	3.999
CaO	9.344	8.897	9.467	9.575	9.211	9.108
K₂O	1.676	0.203	0.003	0.116	0.158	0.13
Cr₂O₃	0.031	0	0	0	0	0.036
NiO	0	0	0	0	0	0
Total	100.647	99.215	98.356	99.843	99.134	99.092
Si	2.818	2.7	2.797	2.816	2.833	2.826
Ti	0.001	0	0	0	0.001	0
Al	1.216	1.305	1.188	1.172	1.17	1.18
Cr	0	0	0	0	0.001	0.001
Fe	0	0	0	0	0.003	0.005
Mn	0.001	0.001	0	0	0	0
Mg	0	0	0	0	0.001	0
Ca	0.2	0.212	0.192	0.184	0.185	0.191
Na	0.837	0.768	0.823	0.82	0.797	0.789
K	0.011	0.12	0	0.007	0.009	0.007
An (%)	19.088	21.425	18.884	18.174	18.703	19.379
Ab (%)	79.837	77.413	81.1	81.179	80.39	79.871

Or (%)	1.075	1.162	0.017	0.647	0.907	0
---------------	-------	-------	-------	-------	-------	---

Santa Terezinha pluton - Clast plagioclase										
	1	2	3	4	5	6	7	8	9	10
SiO₂	64.035	64.909	63.822	64.047	63.563	62.283	62.909	61.447	61.138	56.979
TiO₂	0.004	0.027	0.009	0.001	0.000	0	0.032	0.022	0.027	0.031
Al₂O₃	22.396	21.689	22.328	22.204	22.887	21.766	23.051	22.443	22.948	21.493
FeO	0.02	0.034	0.33	0.038	0	0.04	0.024	0.281	0.034	0
MnO	0.021	0.038	0.035	0	0.023	0.033	0.01	0.002	0	0.023
MgO	0	0.01	0.025	0	0	0	0	0.009	0	0
Na₂O	3.689	3.598	3.275	2.77	4.033	3.418	3.903	3.828	4.059	3.89
CaO	9.476	9.43	9.482	9.738	9.057	6.987	9.012	9.295	9.099	8.991
K₂O	0.155	0.14	0.129	0.297	0.247	4.48	0.284	0.219	0.144	0.184
Cr₂O₃	0	0	0	0.054	0.027	0.061	0	0	0.025	0.005
NiO	0	0	0	0	0	0	0	0	0	0
Total	99.796	99.875	99.435	99.149	99.837	99.068	99.22456	97.546	97.474	91.596
Si	2.834	2.875	2.835	2.846	2.818	2.806	2.805	2.779	2.768	2.734
Ti	0	0.001	0	0	0	0	0.001	0.001	0.001	0.001
Al	1.168	1.132	1.169	1.163	1.196	1.156	1.211	1.196	1.225	1.216
Cr	0	0	0	0.002	0.001	0.002	0	0	0.001	0
Fe	0.001	0.001	0.012	0.001	0	0	0.001	0	0	0
Mn	0.001	0.001	0.001	0	0.001	0.001	0	0.001	0	0.001
Mg	0	0.001	0.002	0	0	0	0	0	0	0
Ca	0.175	0.171	0.156	0.132	0.192	0.165	0.186	0.185	0.197	0.002
Na	0.813	0.81	0.817	0.839	0.779	0.61	0.779	0.815	0.799	0.837
K	0.009	0.008	0.007	0.017	0.014	0.258	0.016	0.013	0.008	0.011
An (%)	17.549	17.274	15.908	13.352	19.467	15.975	18.993	18.308	19.612	19.088

Ab (%)	81.573	81.926	83.346	84.943	79.113	59.094	79.361	80.445	79.559	79.837
Or (%)	0.878	0.8	0.746	1.705	1.42	24.931	1.646	1.247	0.828	1.075

ANEXO II – Análise geoquímica do plúton Catingueira – clasto e matriz de K-feldspato e plagioclásio

Catingueira pluton - clast K-feldspar														
	1	2	3	4	5	6	7	8	9	10	11	12	14	15
SiO₂	63.651	63.643	63.113	63.782	63.642	63.417	63.107	63.931	63.635	63.887	63.562	63.768	63.800	63.368
TiO₂	0.013	0.027	0.058	0	0	0.049	0	0	0	0.004	0.031	0	0.04	0
Al₂O₃	19.995	19.821	19.850	19.984	19.833	19.857	19.594	19.797	19.727	19.922	19.863	19.876	19.922	19.820
FeO	0.008	0	0	0	0.008	0	0.01	0	0.032	0.032	0.051	0.024	0.012	0.059
MnO	0.016	0.018	0	0	0.046	0	0	0	0	0.022	0.008	0	0	0
MgO	0	0.027	0	0	0	0.017	0	0.009	0.001	0	0	0	0	0.004
Na₂O	0	0	0	0	0	0	0.004	0	0	0	0	0	0.001	0
CaO	0.759	0.677	0.763	1.081	0.892	1.39	0.909	0.911	0.542	0.737	0.767	0.795	1.299	0.943
K₂O	15.452	15.863	15.451	14.79	15.389	14.799	15.315	15.504	16.006	15.58	15.634	15.43	15.217	15.145
Cr₂O₃	0	0	0	0	0	0	0	0	0	0	0	0	0	0
NiO	0	0	0	0	0	0	0	0	0	0	0	0	0	0
Total	99.8934	100.075	99.2342	99.6363	99.80952	99.5294	98.9389	100.151	99.94383	100.184	99.946	99.893	100.291	99.339
Si	2.935	2.929	2.929	2.945	2.935	2.924	2.935	2.938	2.936	2.938	2.93	2.94	2.92	2.936
Ti	0	0.001	0.002	0	0	0.002	0	0	0.001	0.001	0.001	0	0.001	0
Al	1.087	1.086	1.086	1.087	1.078	1.079	1.074	1.072	1.073	1.08	1.079	1.08	1.075	1.082
Cr	0	0	0	0	0	0	0	0	0	0	0	0	0	0
Fe	0	0	0	0	0	0	0	0	0	0	0	0	0	0
Mn	0.001	0.001	0	0	0.002	0	0	0	0	0.001	0	0	0	0
Mg	0	0.002	0	0	0	0.001	0	0.001	0	0	0	0	0	0
Ca	0	0	0	0	0	0	0	0	0	0	0	0	0	0
Na	0.068	0.06	0.069	0.097	0.08	0.124	0.082	0.081	0.048	0.066	0.069	0.071	0.115	0.085
K	0.909	0.931	0.915	0.871	0.905	0.87	0.909	0.909	0.942	0.914	0.919	0.908	0.888	0.895

An (%)	0	0	0	0	0	0	0.02	0	0	0	0	0	0.005	0
Ab (%)	6.947	6.091	6.981	9.998	8.096	12.491	8.272	8.198	4.894	6.707	6.939	7.262	11.483	8.645
Or (%)	93.053	93.909	93.019	90.002	91.904	87.509	91.707	91.802	95.106	93.293	93.061	92.738	88.512	91.355

Catingueira pluton - clast K-feldspar														
	16	17	18	19	20	21	22	23	24	25	26	27	28	
SiO₂	61.762	63.379	63.232	62.430	63.449	63.432	62.802	63.080	62.829	61.737	61.480	61.535	61.736	
TiO₂	0.004	0	0.04	0.054	0.058	0.013	0.036	0	0.072	0.04	0.04	0	0.018	
Al₂O₃	19.297	19.901	20.030	20.005	20.154	19.738	19.650	19.503	19.997	19.801	19.913	19.850	19.678	
FeO	0.047	0.01	0	0.15	0.004	0	0.142	0.032	0.024	0.54	0.095	0	0.057	
MnO	0.014	0.006	0	0.026	0.014	0.018	0.016	0.004	0	0.28	0	0	0.02	
MgO	0	0	0.003	0	0	0	0	0	0	0	0	0	0	
Na₂O	0	0.012	0	0.001	0	0	0	0	0	0.004	0.071	0	0	
CaO	0.525	0.615	0.797	0.344	0.864	1.193	0.332	0.582	0.569	0.362	2.503	0.872	2.07	
K₂O	15.738	15.533	15.471	15.905	15.497	15.218	16.097	15.568	15.73	15.915	13.987	15.238	14.139	
Cr₂O₃	0	0	0	0	0	0	0	0	0	0	0	0	0	
NiO	0	0	0	0	0	0	0	0	0	0	0	0	0	
Total	97.387	99.456	99.57337	98.914	100.04	99.612825	99.07551	98.76922	99.22	98.679	98.0889	97.4949	97.71826	
Si	2.923	2.938	2.923	2.913	2.918	2.925	2.927	2.945	2.919	2.89	2.851	2.901	2.883	
Ti	0	0	0.001	0.002	0.002	0	0.001	0	0.003	0.001	0.001	0	0.001	
Al	1.076	1.087	1.091	1.1	1.093	1.073	1.079	1.073	1.095	1.092	1.088	1.103	1.083	
Cr	0	0	0	0	0	0	0	0	0	0	0	0	0	
Fe	0	0	0	0	0	0	0	0	0	0	0	0	0	
Mn	0.001	0	0	0.001	0.001	0.001	0.001	0	0	0.011	0	0	0.001	
Mg	0	0	0	0	0	0	0	0	0	0	0	0	0	
Ca	0	0.001	0	0	0	0	0	0	0	0.004	0			

Na	0.048	0.055	0.071	0.031	0.077	0.107	0.03	0.053	0.051	0.033	0.225	0.08	0.187
K	0.95	0.918	0.912	0.947	0.909	0.895	0.957	0.927	0.932	0.95	0.827	0.916	0.842
An (%)	0	0.061	0	0.005	0	0	0	0	0	0.02	0.334	0	0
Ab (%)	4.825	5.672	7.261	3.182	7.811	10.646	3.039	5.376	5.211	3.341	21.31	8.001	18.2
Or (%)	95.175	94.267	92.739	96.813	92.189	89.354	96.961	94.624	94.789	96.639	78.356	91.999	81.8

Catingueira pluton - Clast plagioclase		
	1	2
SiO₂	63.948	63.728
TiO₂	0.000	0
Al₂O₃	22.019	22.489
FeO	0.25	0.046
MnO	0.04	0.012
MgO	0.044	0
Na₂O	3.225	3.801
CaO	9.738	9.402
K₂O	0.285	0.152
Cr₂O₃	0	0
NiO	0	0
Total		
Si	2.832	2.825
Ti	0	0
Al	1.149	1.175
Cr	0	0

Fe	0	0.002
Mn	0.002	0
Mg	0.003	0
Ca	0.153	0.181
Na	0.836	0.808
K	0.016	0.009
An (%)	15.222	18.103
Ab (%)	83.176	81.035
Or (%)	1.602	0.862

Catingueira pluton - Clast plagioclase							
	1	2	3	4	5	6	7
SiO₂	62.550	62.451	61.514	62.020	62.281	62.342	62.451
TiO₂	0.035	0.009	0	0	0	0	0.04
Al₂O₃	24.371	24.393	24.803	24.704	23.640	23.373	23.410
FeO	0.024	0.049	0.04	0.269	0.036	0.04	0.016
MnO	0	0.022	0	0.058	0.018	0	0.062
MgO	0.024	0	0	0.014	0.002	0	0
Na₂O	3.82	3.431	4.06	4.122	4.186	4.085	3.933
CaO	9.592	9.211	9.19	9.292	9.131	9.507	9.294
K₂O	0.093	0.418	0.22	0.156	0.116	0.159	0.244
Cr₂O₃	0.036	0	0.061	0.036	0.029	0	0
NiO	0	0.091	0.002	0	0	0	0
Total	100.545	100.074	99.890	99.439	99.439	99.506	99.450
Si	2.739	2.753	2.715	2.718	2.767	2.76	2.771
Ti	0.001	0	0	0	0	0	0.001
Al	1.258	1.267	1.29	1.276	1.238	1.22	1.224
Cr	0.001	0	0.002	0.001	0.001	0	0
Fe	0	0	0	0	0	0	0

Mn	0	0.001	0	0.002	0.001	0	0.002
Mg	0.179	0	0	0.001	0	0	0
Ca		0.162	0.192	0.194	0.199	0.194	0.187
Na	0.814	0.787	0.786	0.79	0.786	0.816	0.8
K	0.005	0.024	0.012	0.009	0.007	0.009	0.014
An (%)	17.944	16.658	19.377	19.515	20.079	19.019	18.691
Ab (%)	81.56	80.926	79.372	79.606	79.259	80.099	79.928
Or (%)	0.52	2.416	1.25	0.879	0.663	0.881	1.381

Catingueira pluton - Matrix plagioclase

	1	2
SiO₂	63.948	63.728
TiO₂	0.000	0
Al₂O₃	22.019	22.489
FeO	0.25	0.046
MnO	0.04	0.012
MgO	0.044	0
Na₂O	3.225	3.801
CaO	9.738	9.402
K₂O	0.285	0.152
Cr₂O₃	0	0
NiO	0	0
Total		
Si	2.832	2.825
Ti	0	0
Al	1.149	1.175
Cr	0	0

Fe	0	0.002
Mn	0.002	0
Mg	0.003	0
Ca	0.153	0.181
Na	0.836	0.808
K	0.016	0.009
An (%)	15.222	18.103
Ab (%)	83.176	81.035
Or (%)	1.602	0.862